# Analyzing the Li-Al-O Interphase of Atomic Layer Deposited Al<sub>2</sub>O<sub>3</sub> Films on Layered Oxide Cathodes Using Atomistic Simulations

Julie A. Nguyen, Abigayle Becker, Krishan Kanhaiya, Hendrik Heinz\*, and Alan W. Weimer\*

Department of Chemical and Biological Engineering, University of Colorado Boulder, Boulder, CO 80309, USA

\*Corresponding authors: alan.weimer@colorado.edu, hendrik.heinz@colorado.edu

Keywords: atomic layer deposition, molecular dynamics, atomistic simulation, thin film, Al<sub>2</sub>O<sub>3</sub>, lithium-ion battery, layered transition metal oxide, LiAlO<sub>2</sub>

(Surfaces, Interfaces, and Applications section)

#### **ABSTRACT**

Alumina surface coatings are commonly applied to layered oxide cathode particles for lithiumion battery applications. Atomic layer deposition (ALD) is one such surface coating technique and ultrathin alumina ALD films (< 2 nm) are shown to improve the electrochemical performance of LiNi<sub>x</sub>Mn<sub>y</sub>Co<sub>1-x-y</sub>O<sub>2</sub> materials, with groups hypothesizing that a beneficial Li-Al-O product is being formed during the alumina ALD process. However, the atomic structure of these films is still not well understood and quantifying the interface of ultrathin (~1 nm) ALD films is an arduous experimental task. Here, we perform molecular dynamics simulations of amorphous alumina films of varying thickness in contact with the (0001) LiCoO<sub>2</sub> (LCO) surface to quantify the film nanostructure. We calculate elemental mass density profiles through the films and observe the Li-Al-O interphase extends for ~2 nm from the LCO surface. Additionally, we observe layering of Al and O atoms at the LCO-film interface that extends for ~1.5 nm. To access the short-range order of the amorphous film, we calculate the Al coordination numbers through the film. We find that while [4]Al is the prevailing coordination environment, significant amounts of [6]Al exist at the interface between the LiCoO<sub>2</sub> surface and the film. Taken together, these principal findings point to a pseudomorphic Li-Al-O overlayer that approximates the underlying layered LiCoO2 lattice but does not exactly replicate it. Additionally, with sufficient thickness, the Li-Al-O film transitions to an amorphous alumina structure. We anticipate our findings on the ALD-like, Li-Al-O film nanostructure can apply to other layered LiNi<sub>x</sub>Mn<sub>y</sub>Co<sub>1-x-y</sub>O<sub>2</sub> materials because of their shared crystal structure with LiCoO<sub>2</sub>. This work provides insight into the nanostructure of amorphous ALD alumina films to help inform their use as protective coatings for Li-ion battery cathode active materials.

# 1. INTRODUCTION

The positive electrode, which contains the cathode active material, determines the energy density of the Li-ion battery<sup>1-3</sup> and different chemical formulations of this material—especially for the layered transition metal oxide, LiNi<sub>x</sub>Mn<sub>y</sub>Co<sub>1-x-y</sub>O<sub>2</sub> or NMC,—allow for increased access to the lithium inventory. However, layered transition metal oxides experience structural disordering and/or particle cracking during electrochemical cycling.<sup>4-8</sup> This structural degradation manifests on the macroscale as significant capacity fade and/or power fade.<sup>2, 9, 10</sup>

Surface coatings are frequently added to transition metal oxides to improve electrochemical performance for Li-ion battery applications. The surface coatings impart benefits such as reducing capacity fade and extending cycling stability. 11-14 Coating methods range from wet chemical 15-17 to atomic layer deposition (ALD), 11-13, 18-22 with alumina surface coatings being commonly deposited for both techniques. To be electrochemically beneficial to transition metal oxides, wet chemical Al<sub>2</sub>O<sub>3</sub> coatings require post-process heat treatment. Moreover, researchers agree that this high temperature heat treatment leads to the formation of an advantageous Li-Al-O phase at the interface between the transition metal oxide and Al<sub>2</sub>O<sub>3</sub> coating. 16, 17, 23, 24 The Li-Al-O phase is electrochemically beneficial because LiAlO<sub>2</sub> promotes Li-ion conductivity over pure Al<sub>2</sub>O<sub>3</sub>. 12, 17 Interestingly, ALD coatings do not require annealing to provide electrochemical improvements. 12, 23, 25 In particular, researchers have shown that annealing does not significantly change the electrochemical performance of Al<sub>2</sub>O<sub>3</sub> ALD coated NMC532. 23

ALD coatings' ability to provide electrochemical benefits without annealing poses the open question of *why* ALD coatings are beneficial to layered transition metal oxides. Researchers have demonstrated the ALD film can serve as a physical barrier from the electrolyte, <sup>19</sup> scavenge HF from the electrolyte, <sup>26</sup> adjust the redox states of the transition metals, <sup>27</sup> and remove surface

species.<sup>22, 28</sup> More broadly, atomic layer deposition is of interest to the electrochemical storage community because of its ability to engineer the interface on a variety of energy materials.<sup>29</sup> ALD grows conformal, pin-hole free thin films on substrates with sufficient ALD cycles.<sup>30</sup> Generally, one ALD cycle is comprised of two self-limiting gas-solid phase reactions separated by purge steps. Using the trimethylaluminum (TMA)/water chemistry as an example, one ALD cycle consists of the introduction of TMA to the substrate, followed by an inert gas purge to remove byproducts and excess unreacted TMA, then the introduction of water to the substrate, and finally another inert gas purge. A subset of ALD is particle ALD, where conformal films are grown on fluidized particles.<sup>31, 32</sup> Particle ALD is commonly used on cathode active materials. Whereas annealed wet chemical Al<sub>2</sub>O<sub>3</sub> coatings are on the order of tens of nanometers thick, electrochemically beneficial ALD Al<sub>2</sub>O<sub>3</sub> films using the TMA/water chemistry are < 1 nm thick, which equates to roughly 2-6 ALD cycles.<sup>25, 33</sup>

Hoskins et al. cast doubt on the previous understanding that an abrupt interface exists between the transition metal oxide substrate and alumina ALD film.<sup>33</sup> They performed alumina ALD on NMC111 powders and used low energy ion scattering (LEIS) and time of flight mass spectrometry (ToF-SIMS) to show lithium is present on the surface of the ALD films while the transition metal sites were completely covered. They partly attributed this phenomenon to a Li-Al-O product. Additionally, they performed alumina ALD on LiOH, a common surface contaminant found on NMC materials. Hoskins et al. observed atypically elevated aluminum deposition on LiOH, which is indicative of a non-ALD reaction during the first ALD cycle. They hypothesized this non-ALD reaction led to the formation of LiAlO2 rather than Al<sub>2</sub>O<sub>3</sub>. The work of Hoskins et al. provides evidence for a reactive interface between the transition metal oxide substrate and alumina ALD

film, where a new, stable Li-Al-O compound is formed. Put another way: at low ALD cycle counts, the alumina ALD process on LiMO<sub>2</sub> does not grow pure alumina films, but rather Li-Al-O films.

Previous literature investigated the quality and stoichiometry of amorphous Li-Al-O films with widely varying results. Liu et al. investigated the lithiation of alumina films by galvanostatically cycling an Al nanowire anode in a lithium cell. They observed that the native, 4-5 nm thick Al<sub>2</sub>O<sub>3</sub> surface layer of the wire experienced an irreversible lithiation, creating a Li-Al-O product.<sup>34</sup> Other groups addressed the question of how many Li atoms an Al<sub>2</sub>O<sub>3</sub> lattice can accommodate. For example, Li<sub>2</sub>O-Al<sub>2</sub>O<sub>3</sub> ALD films grown by Aaltonen et al. achieved a Li/Al ratio of 1.6 in the bulk film and a Li/Al ratio of 2.2 at the film surface.<sup>35</sup> However, Comstock & Elam grew LiAlO<sub>x</sub> ALD films and found it difficult to make thick films with the correct stoichiometry. Their thin films achieved a Li/Al ratio of 0.82; their thick films could only achieve a Li/Al ratio of 0.55.<sup>36</sup> Jung & Han utilized ab-initio molecular dynamics simulations to suggest that Li<sub>3.4</sub>Al<sub>2</sub>O<sub>3</sub> is the thermodynamically most favorable compound.<sup>37</sup> The authors of that study went on to propose the electrolyte lithiates the Al<sub>2</sub>O<sub>3</sub> coating in Li-ion batteries. In the context of an Al<sub>2</sub>O<sub>3</sub> coating on a lithium-containing LiMO<sub>2</sub> material, the more likely scenario is that the cathode active material provides the initial lithiation of the film. Indeed, Young et al. provided evidence for lithiation of a nucleating alumina film during the ALD process. They observed the formation of a Li-rich surface on LiMn<sub>2</sub>O<sub>4</sub> after one cycle of TMA/H<sub>2</sub>O using X-ray photoelectron spectroscopy (XPS).<sup>22</sup> The lithium exhibited dynamic behavior and "breathed" away from and to the LiMn<sub>2</sub>O<sub>4</sub> surface during the TMA and H<sub>2</sub>O doses, respectively. Assuming all Li detected by XPS belonged to the surface layer, the stoichiometry was Li<sub>0.33</sub>Al<sub>1.89</sub>O<sub>3</sub>. The Li/Al ratio provides a general indicator of film type but lacks the insight into the film nanostructure. Additionally, there is considerable variation in the observed or predicted Li/Al ratio in the Li-Al-O film, with values as low as 0.17 and as high as 2.2.

While ALD surface coatings are increasingly applied to the cathode active material of Li-ion batteries, the theoretical arguments for why a thin alumina ALD film is beneficial are still being worked out. The existence of an Li-Al-O interphase between a layered transition metal oxide surface and alumina coating deposited by wet-chemical methods is well established. 16, 17, 23, 24 However, the interphase for ultrathin alumina ALD coatings is not as well studied. Our present work uses molecular dynamics (MD) simulations to investigate an ALD-like alumina film in contact with a layered lithium transition metal oxide surface. We theorize the resulting Li-Al-O interphase is crucial to explaining the benefit of alumina ALD on the layered oxide class of cathode materials. In addition, we compare the predicted atomic structure of this Li-Al-O interphase to experimental coordination values and other simulation studies. We hypothesize that at low ALD cycle counts, the layered lithium transition metal oxide surface serves as a template for a pseudomorphic, layered Li-Al-O film. By extension of this hypothesis, we conjecture that after sufficient ALD cycles, the film structure transitions to the conventionally observed amorphous Al<sub>2</sub>O<sub>3</sub> ALD coating.

# 2. METHODOLOGY

A non-bonded α-Al<sub>2</sub>O<sub>3</sub> model and a bonded LiCoO<sub>2</sub> (LCO) atomistic model were used to simulate the film-layered cathode oxide interface. Both models were parameterized using the CVFF form of the INTERFACE Force Field (IFF),<sup>38</sup> where the potential energy is represented by Eqn. 1. Table S1 lists the parameters for each model. Typical deviations in lattice parameters are less than 1% relative to experiment; surface energies and elastic moduli deviate less than ~5% from experimental measurements.<sup>39-42</sup>

$$E_{potential} = \sum_{ij \, bonded} K_{r,ij} \left( r_{ij} - r_{0,ij} \right)^{2}$$

$$+ \sum_{ijk \, bonded} K_{\theta,ij} \left( \theta_{ijk} - \theta_{0,ijk} \right)^{2}$$

$$+ \sum_{(1,2 \, and \, 1,3 \, excl)} \varepsilon_{0,ij} \left( \left( \frac{\sigma_{ij}}{r_{ij}} \right)^{12} \right)^{2}$$

$$- 2 \left( \frac{\sigma_{ij}}{r_{ij}} \right)^{6} + \frac{1}{4\pi \varepsilon_{0} \varepsilon_{r}} \sum_{(1,2 \, and \, 1,3 \, excl)} \frac{q_{i}q_{j}}{r_{ij}}$$

$$(1)$$

The (0001) LCO surface was studied because it is the lowest energy surface for layered transition metal oxides. <sup>43-45</sup> Physically, layered LiMO<sub>2</sub> particles that display a considerable amount of the (0001) surface facet appear as flat, hexagonal plates. <sup>43</sup> The non-bonded Al<sub>2</sub>O<sub>3</sub> model was chosen because it facilitated the generation and reconstruction of amorphous Li-Al-O films during annealing in molecular dynamics simulations.

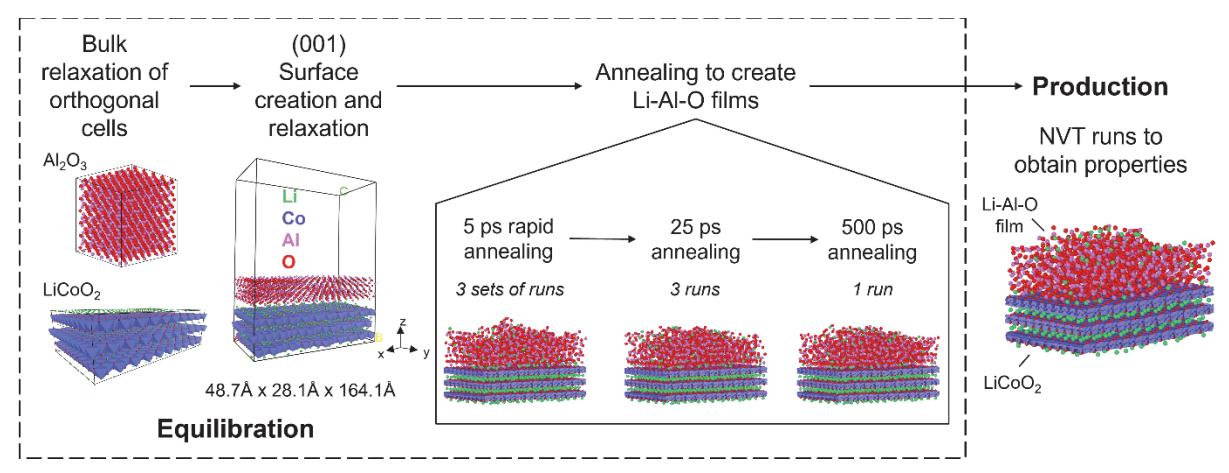


**Figure 1.** Simulation workflow used to generate amorphous Li-Al-O films in contact with the (0001) LiCoO<sub>2</sub> surface. For simplicity, the simulation cells were used as orthogonal supercells with equivalent (001) surfaces. The equilibration routine consisted of relaxing the bulk Al<sub>2</sub>O<sub>3</sub> and LiCoO<sub>2</sub> cells at 393 K, converting them into (001) surfaces, and running a series of annealing simulations to randomly generate amorphous Li-Al-O films in contact with LCO. The production NVT runs occurred at 393 K for 500 ps and these trajectories were used for analysis. Analyzed properties included overall film densities, lithium incorporation energies, element mass density profiles, bond length, and atom coordination. Here, Li atoms are colored green, Co as blue, Al as pink, and O as red.

Figure 1 shows the simulation workflow. A multi-step equilibration routine was employed to generate equilibrium structures that were then analyzed in the production simulations. For all dynamics simulations, a 12 Angstrom van der Waals cutoff was used for pairwise Lennard-Jones interactions. The summation of long-range electrostatic interactions was carried out with the Ewald method when using Materials Studio and with the PPPM K-space solver when using LAMMPS,<sup>46</sup> both in high accuracy of 10<sup>-4</sup>. The subsequent sections explain the simulation workflow in detail.

# 2.1 Bulk relaxation and (0001) surface creation

The (0001) surface creation was as follows: the trigonal unit cells of LiCoO<sub>2</sub> and Al<sub>2</sub>O<sub>3</sub> were converted to orthogonal cells, then to equivalent (001) surfaces. The (001) LiCoO<sub>2</sub> surface was created by first relaxing the bulk structure (2x3x1 orthogonal supercell) in Materials Studio using the NPT ensemble (velocity scale thermostat, Parrinello barostat) with a 0.5 fs timestep for

100 ps at 393 K and 0.0001 GPa. The 393 K temperature was chosen to replicate the experimental ALD conditions of Hoskins et al.<sup>33</sup> A (001) LCO surface was formed by creating a 5x5x1 supercell that is 14.1 Å thick in the z direction, adding 150 Angstroms of vacuum space in the z direction, and moving half of the Li atoms from the bottom LCO surface to the top to prevent a charge dipole from forming. Additionally, the LCO surface was further relaxed by running six simulations in the NVT ensemble (velocity scale thermostat, Materials Studio Discover module) at 393 K with a 1 fs timestep for 100 ps each. The (001) Al<sub>2</sub>O<sub>3</sub> surface was created by first relaxing the bulk structure (3x5x2 orthogonal supercell) in LAMMPS using the NPT ensemble (Nosé-Hoover thermostat and barostat) with a 0.5 fs timestep for 100 ps at 393 K and 1.0 atm. The equilibrium orthogonal unit cell lattice vectors were determined by averaging the last 50 ps of the NPT run. A (001) Al<sub>2</sub>O<sub>3</sub> surface was formed by creating a 6x6x1 orthogonal supercell, adding 150 Angstroms of vacuum space in the z direction, and moving half of the Al atoms from the bottom surface to the top surface to prevent a charge dipole from forming.

# 2.2 Annealing simulations to create amorphous Li-Al-O films

Typical alumina ALD has been reported to have a growth per cycle (GPC) of anywhere between 0.9 Å/ALD cycle<sup>30</sup> to 1.2 Å/ALD cycle.<sup>47</sup> It is important to note that GPC is affected by temperature and the substrate the ALD is being performed on.<sup>30, 48</sup> The alumina GPC on layered cathode oxide materials like LCO and NMC is elevated with groups reporting GPCs as large as 2.2 Å/ALD cycle.<sup>12, 33</sup> One monolayer of α-Al<sub>2</sub>O<sub>3</sub> has a z-height of 2.2 Å. From that standpoint, the MD simulations of this current work capture a growth per cycle of 2.2 Å/ALD cycle, where one Al<sub>2</sub>O<sub>3</sub> monolayer equates to one ALD cycle. However, as we will see later in this paper, one simulated Al<sub>2</sub>O<sub>3</sub> monolayer does not produce a fully formed film.

Molecular dynamics simulations utilized a 48.7 Å x 29.1 Å x 164.1 Å orthogonal cell containing a (001) LCO surface and with a (001) Al<sub>2</sub>O<sub>3</sub> surface (variable number of monolayers) brought in contact. Amorphous Li-Al-O films in contact with LiCoO2 were generated using an annealing protocol in LAMMPS. There are infinite possibilities when generating amorphous structures. Thus, to make the computation tractable, we performed a series of annealing simulations, which are commonly utilized when randomly generating amorphous structures.<sup>49, 50</sup> We then selected the lowest energy structure for the production run and extracted properties from this final simulation. The semi-automated annealing protocol consisted of three sets of 5 ps NVT simulations (canonical velocity rescaling thermostat, <sup>51</sup> 1 fs timestep), three 25 ps NVT simulations, and one 500 ps NVT simulation. It is important to note that the simulated annealing was used to generate structures that were comparable to experimental ALD films, but the annealing protocol was not used as a re-creation of an actual physical process. During simulated annealing, the bottom layer of Li atoms of the LCO surface furthest from the Al-O film was held fixed. An annealing simulation began at a high temperature (thousands of Kelvins) and cooled down to 393 K. The highest temperature selected for each monolayer system was either 3000 K or 4000 K and successive 5 ps runs were 1000 K less than the previous simulation, with the last temperature of the set beginning at 1000 K. Similar protocols were used previously to obtain equilibrium distributions of alkali ions and earth alkali ions in clay and cement minerals.<sup>52,53</sup> After these three rapid annealing sets, three longer annealing NVT simulations were conducted at 25 ps each. The first 25 ps simulation began at 3000 K and had a temperature ramp rate of -104 K/ps, the second began at 2000 K and ramped -64 K/ps, and the third began at 1000 K and ramped -24 K/ps. A final, 500 ps NVT simulation was used to equilibrate the structure. The 500 ps equilibration simulation began at 1000 K and ramped -1 K/ps.

Additional simulations were run for the 10-monolayer systems. The Li-Al-O replicates 1-3 followed the annealing protocol previously specified while an amorphous Al-O film with minimal lithium distribution was generated by freezing the LCO slab and running a 100 ps NVT simulation at 2,000 K, then unfreezing all atoms and running a 1 ns NVT simulation at 393 K. A fifth structure was generated to have a homogeneous lithium distribution through the Li-Al-O film lattice by running a 100 ps NVT simulation at 2,000 K, followed by a 1 ns NVT simulation at 393 K.

# 2.3 Simulations used to generate properties for analysis

Once equilibrated structures were obtained, the production simulations were conducted in the NVT ensemble at 393 K using LAMMPS (canonical velocity rescaling thermostat, 1 fs timestep) for 500 ps. Properties calculated from these production runs include overall film densities, lithium incorporation energies, film energies, element mass density profiles, bond length, and atom coordination.

# 2.3.1 Calculation of film density

The simulated, bulk film densities were calculated by approximating the film geometry as a rectangular prism. The film surface, which included the top ~5-7 Å atoms in contact with vacuum, was excluded. Then, the number of Al atoms were counted in this rectangular prism and divided by two to obtain an approximate number of Al<sub>2</sub>O<sub>3</sub> units. Then, this mass was divided by the volume of the rectangular prism to obtain the density (Figure S1 shows an example). The plotted film densities (Figure 2h) were calculated every 50 ps of the 500 ps trajectories and averaged. A single monolayer does not form a continuous film and was excluded from the film density analysis.

# 2.3.2 Calculation of lithium inclusion energy

The energy of lithium inclusion in the Al-O structure was calculated from single point energies as a difference between the film-cathode system, the equilibrated pure LCO surface and the Al-O film (which is the equilibrated Al-O structure of the film-cathode system with the lithium atoms removed). For every monolayer system, the Li inclusion energy was calculated for three different amorphous Li-Al-O structures and averaged (Figure 3a). These values serve as a first qualitative estimate and dynamic trajectories with extensive sampling can be utilized in future work for quantitative analysis.

# 2.3.3 Calculation of film energy

The film energy per Al<sub>2</sub>O<sub>3</sub> unit was calculated by subtracting the total energy of the LCO surface from the total energy of each 10-monolayer system, dividing that difference by the simulated cross-sectional surface area, then dividing by the number of simulated Al<sub>2</sub>O<sub>3</sub> units (Figure 3d).

# 2.3.4 Calculation of elemental mass density profiles

The density profile tool for VMD<sup>54</sup> was used to calculate the lithium, aluminum, and oxygen mass density profiles in the z-direction away from the LCO surface (Figure 4). A  $\Delta z$  of 0.1 Å was used and the density profiles were averaged across the entire 500 ps trajectory (1000 frames) for each monolayer system.

# 2.3.5 Calculation of bond length

Bond lengths were calculated by finding the maximum of the first nearest neighbor shell of the calculated partial radial distribution function (pRDF) for each bond type. We used OVITO<sup>55</sup> to calculate the partial radial distribution functions. The normalized partial radial distribution

function is given by Eqn. 2, where we select a particle of type  $\alpha$  as the origin, r = 0, and sweep out a control spherical volume with radius r and thickness  $\Delta r$ :

$$g_{\alpha\beta}(r) = \frac{\langle N_{\alpha\beta}(r, \Delta r) \rangle}{\frac{N_{\beta}}{V} 4\pi r^2 \Delta r}$$
 (2)

where  $\langle N_{\alpha\beta}(r,\Delta r)\rangle$  is the ensemble averaged number of  $\beta$  particles between a distance of r and  $r+\Delta r$  from particle  $\alpha$ . The number density for particle  $\beta$  in the system volume, V, is given by  $\frac{N_{\beta}}{V}$ . The pRDFs with a cutoff of 12 Angstroms and  $\Delta r$  of 0.1 Å were calculated for each film system every 100 frames (50 ps) for 1000 frames (500 ps) and averaged. The standard deviations of the bond lengths were calculated as the full width at half maximum for the first maximum of each pRDF. Only the atoms part of the film region (and not the interior LiCoO<sub>2</sub> sheets) were included in the analysis. The average bond lengths for Al-O, O-Li, and O-O are summarized in Table 1. The cumulative radial distribution functions and pRDFs for each monolayer system are included in Figures S2 to Figure S8 in the Supporting Information.

# 2.3.6 Calculation of coordination numbers

The coordination number was calculated by integrating the partial radial distribution function over a distance—the coordination number is essentially the number of particles within that distance. For a particle of type  $\alpha$  in the  $\alpha$ - $\beta$  bond, the coordination number was defined as:

$$N_{\alpha\beta} = \frac{4\pi N_{\beta}}{V} \int_{0}^{r_{cutoff}} r^{2} g_{\alpha\beta}(r) dr$$
 (3)

We used OVTIO to calculate the coordination numbers by applying a shorter cutoff,  $r_{cutoff}$ , which was equal to the first minimum of that bond type's pRDF. For example, the coordination numbers for Al and O in the Al-O bond of the four-monolayer system were calculated using a cutoff of 2.45

Å, which equals the first minimum of the  $g_{Al-O}$  pRDF for that system. The coordination numbers were calculated every 100 frames (50 ps) for 1000 frames (500 ps) and averaged. The standard deviations were on the order of  $\pm 1$ -5% of atoms for each coordination number, with Li having the largest standard deviations for the thinnest monolayer systems.

#### 2.4 Limitations and uncertainties

The models used in the simulations assume an alumina phase with no hydration, which is a good first approximation of ALD experiments, and the reported trends are expected to remain semi-quantitatively the same under experimental conditions. The force fields for LCO and alumina have excellent reproduction of structural and energetic properties. These properties have less than 1% deviation in computed geometries and < 10% deviation in computed energy differences, 39-42 which is consistent with the reliability of IFF for other inorganic chemistries. 56

Under ideal laboratory conditions, the ALD process consists of two separate, surface-limited gas-solid phase reactions. For example, alumina ALD precursor molecules like trimethylaluminum, TMA or Al(CH<sub>3</sub>)<sub>3</sub>, should only react with surface hydroxyl groups to form AlOH surface species. However, deviations from ideality occur in practice. Chemical vapor deposition (CVD) could occur in parallel to ALD if the reaction chamber is not sufficiently purged of excess reactant before the next precursor dose is introduced. Moreover, sufficient TMA/water ALD cycles deposit an alumina film with a certain amount of hydroxyl group impurities.<sup>57</sup> Details of such reactions depend on specific thermodynamic conditions, which are beyond the scope of this paper and can be examined in follow-on studies.

Carbonate and hydroxide contaminants such as Li<sub>2</sub>CO<sub>3</sub> and LiOH exist on the surface of layered transition metal oxides.<sup>58, 59</sup> The presence of these impurities most likely explains the

elevated growth per cycle (GPC) of alumina ALD on layered transition metal oxides.<sup>33</sup> Typical alumina ALD has a GPC of 1.2 Angstrom/ALD cycle.<sup>47</sup> In the case of alumina ALD on layered transition metal oxide materials, the GPC is 2.2 Angstroms/ALD cycle, or *one monolayer per cycle*.<sup>12,33</sup> Our model LiCoO<sub>2</sub> surface does not describe surface contaminants. However, the effect of surface impurities on the resulting alumina ALD film thickness is partially accounted for by correlating one simulated alumina monolayer to one experimental alumina ALD cycle.

#### 3. RESULTS AND DISCUSSION

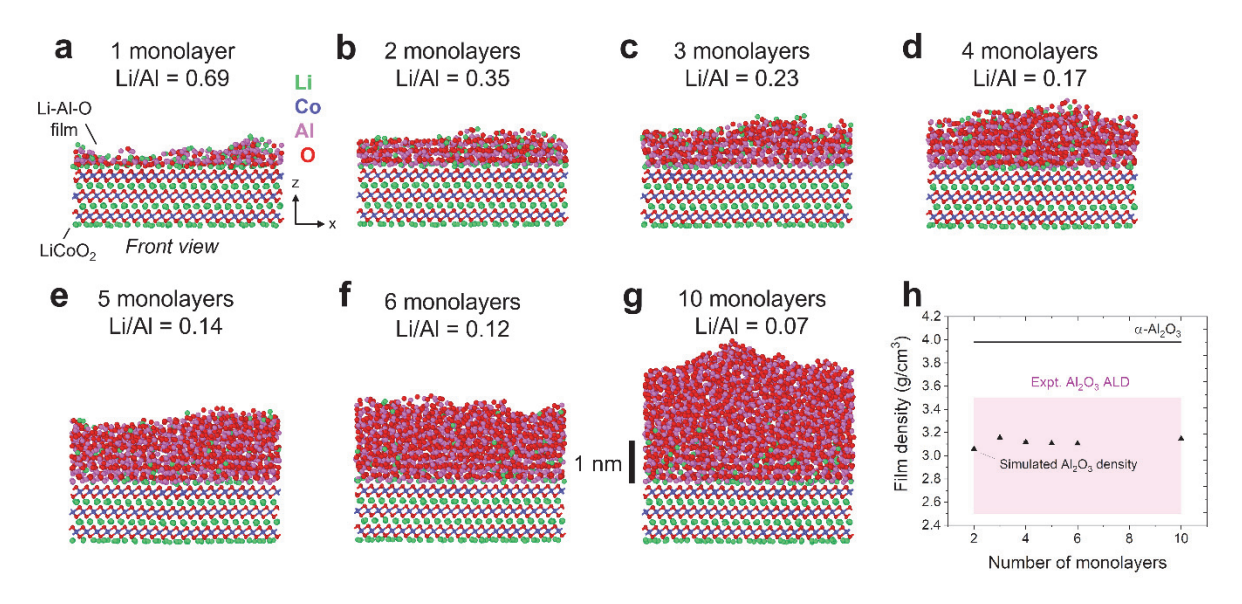


Figure 2. (a-g) The amount of alumina in contact with the (0001) LCO surface varied from one to six and ten  $Al_2O_3$  monolayers. The 10-monolayer system possessed the maximum film thickness of ~3 nm. Here, Li atoms are colored green, Co as blue, Al as pink, and O as red. (h) The densities of the simulated, amorphous alumina films were calculated every 100 frames for the entirety of the 1000 frame production simulations. These densities were averaged and plotted. The simulated alumina density is stable at  $3.12 \pm 0.01$  g/cm<sup>3</sup> across monolayers. The experimental densities for ALD alumina films are shown as the pink region and range from ~2.5 g/cm<sup>3</sup> to ~3.5 g/cm<sup>3</sup> depending on ALD process conditions.<sup>57, 60, 62</sup> The experimental density of α-Al<sub>2</sub>O<sub>3</sub> (3.98 g/cm<sup>3</sup>) is plotted as a solid black line for reference.

Figure 2 provides a visual snapshot of the production simulations. Panels a – g were visualized using OVITO.<sup>55</sup> One to six and 10 stoichiometric alumina layers were simulated in contact with the (0001) LiCoO<sub>2</sub> surface. The snapshots were selected halfway through each 500 ps trajectory (i.e., frame 501). One Al<sub>2</sub>O<sub>3</sub> monolayer consisted of 72 units (144 Al and 216 O atoms). The LiCoO<sub>2</sub> slab consisted of 2400 atoms (600 Li, 600 Co, and 1200 O atoms), with 100 Li atoms present at the surface. One simulated alumina monolayer could be correlated to one alumina ALD cycle—especially if the reported experimental growth per cycle is 2.2 Å/ALD cycle. However, real ALD processes exhibit more nuance: many ALD chemistries experience a delay in

film growth since the film must first nucleate on the substrate material, which may need to be functionalized with active ALD surface groups.  $^{30}$  Additionally, the growth per cycle is affected by the temperature of the ALD process.  $^{30, 60, 61}$  In Figure 2a, the one monolayer simulated film is not continuous. In panels 2a - 2g, lithium is present throughout the entire Al-O lattice for all systems except the 10-monolayer simulation. At 10 alumina monolayers, the Li atoms exist partway through the alumina lattice before the film transitions to a disordered Al-O region.

Figure 2h summarizes the overall density of the films. The density of  $\alpha$ -Al<sub>2</sub>O<sub>3</sub> (3.98 g/cm<sup>3</sup>) is provided as a reference, however, experimental alumina ALD films range in density from ~2.5 g/cm<sup>3</sup> to ~3.5 g/cm<sup>3</sup>.<sup>57, 60, 62</sup> We observe that the simulated film densities fall within the experimental density range reported for alumina ALD. Furthermore, the simulated alumina density is stable across monolayers and the averaged density (2 – 6 and 10 monolayers) is 3.12  $\pm$  0.01 g/cm<sup>3</sup>. These findings indicate that the simulated films are physically representative of experimental alumina films grown by ALD.

# 3.1 Thermodynamic-mechanical argument

From a mechanical standpoint, solid-on-solid film growth generates strain in the resulting film. It has been well-documented that very thin alumina ALD films (< 10 ALD cycles) are beneficial to layered LiMO<sub>2</sub> electrochemical performance. <sup>12, 18, 23, 25, 33, 63</sup> During the initial ALD cycles, the alumina film grows on the substrate surface, rather than a pre-existing alumina film. Misfit strain, which arises from lattice mismatch between the film and the substrate plays an important role in determining the film overlayer structure. <sup>64</sup> Kolasinski defines misfit strain as the difference between the film and substrate lattice vectors divided by the lattice vector of the substrate.

$$\varepsilon_0 = \frac{a_{film} - a_{substrate}}{a_{substrate}} \tag{4}$$

Table S2 lists the lattice vectors for select compounds including  $\alpha$ -Al<sub>2</sub>O<sub>3</sub>,  $\alpha$ -LiAlO<sub>2</sub>, and LiCoO<sub>2</sub>. Indulging in a theoretical exercise using crystalline structures—while acknowledging the actual structure of alumina ALD films is more disordered than crystalline alumina—we use Eqn. 4 to calculate the misfit strain for an  $\alpha$ -Al<sub>2</sub>O<sub>3</sub> film on LCO in the xy plane as 69%. Positive strain indicates the  $\alpha$ -alumina film experiences a compressive strain as it tries to conform to the LCO substrate surface. From a thermodynamic-mechanical standpoint, the large misfit strain between the  $\alpha$  lattice vectors of the  $\alpha$ -Al<sub>2</sub>O<sub>3</sub> and LiCoO<sub>2</sub> unit cells provides a compelling reason for an intermediary structure to exist between LCO and the alumina film. This intermediary structure serves to help relieve the strain that would otherwise accumulate at the interface. Interestingly, the misfit strain for an  $\alpha$ -LiAlO<sub>2</sub> film on LCO is only -0.55%. Negative strain values indicate the film experiences tensile strain. However, since the misfit strain value is so low for  $\alpha$ -LiAlO<sub>2</sub> on LCO, film strain is essentially non-existent, and the two crystal lattices are isomorphic.

Evidence exists for a LiAlO<sub>2</sub> interphase between annealed wet chemical alumina coatings on layered transition metal oxides.  $^{16, 17, 23, 24}$  Previous researchers used  $^{27}$ Al solid-state NMR to demonstrate that the LiAlO<sub>2</sub> interphase exhibits varying amounts of  $\alpha$ -LiAlO<sub>2</sub> character depending on coating conditions.  $^{16, 17, 23}$  Han et al. asserted that  $\alpha$ -LiAlO<sub>2</sub> in particular is beneficial to electrochemical performance because it is lattice matching to NMC and has a higher Li-ion conductivity than  $\gamma$ -LiAlO<sub>2</sub>.  $^{16, 23}$  Zheng et al. used high angle annual dark field scanning transmission electron microscopy (HAADF-STEM) to observe an epitaxial, 7 nm thick  $\alpha$ -LiAlO<sub>2</sub> film that lattice matched the LCO substrate.  $^{24}$  However, electrochemically beneficial alumina films grown by ALD are much thinner (< 1 nm) than films grown by wet chemical methods. Hence, it is experimentally difficult to measure the interphase nanostructure.

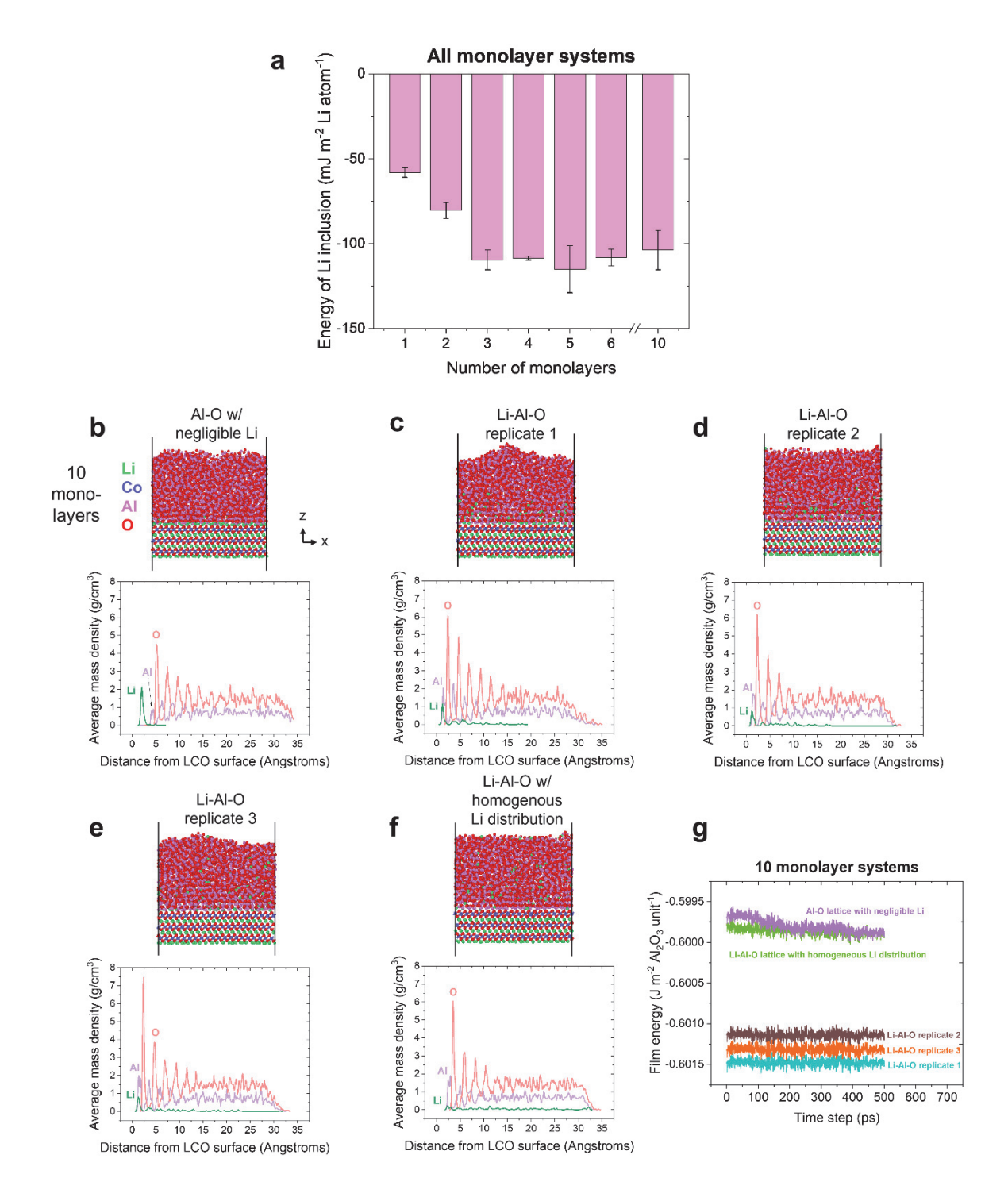


**Figure 3.** (a) The calculated energy, E, of including lithium in the amorphous Al-O lattice using the equation  $E_{Li\ inclusion} = E_{Li-Al-O\ system} - \left(E_{LCO\ surface} + E_{Al-O\ surface}\right)$ , where  $E_{Li\ Al-O\ system}$  is the total energy of the film-LCO system,  $E_{LCO\ surface}$  is the total energy of the LCO surface with no alumina film in contact with it, and  $E_{Al-O\ surface}$  is the total energy of the amorphous Al-O slab after deleting the Li atoms from it. The energy of incorporating Li into the alumina lattice reaches a maximum favorability by three monolayers. The average energy of lithium inclusion in

the Al-O film is -109 mJ m<sup>-2</sup> Li atom<sup>-1</sup>  $\pm$  5 mJ m<sup>-2</sup> Li atom<sup>-1</sup> (excluding the 1- and 2-monolayer simulations). (b-f) The lowest energy 10-monolayer structure was investigated, and snapshots of each trajectory are provided. Average elemental mass densities through the Li-Al-O films were calculated for the entire 1000-frame trajectories of replicates 1-3 and the last 1000 frames of the first and fifth structure trajectory. Lithium extends through the Li-Al-O film replicates for about 2-2.5 nm. The Li average mass density for the fifth structure indicates lithium is homogeneously dispersed through the film. (g) The film energy of the last 500 ps for each trajectory is plotted. The lowest energy trajectory (replicate 1) was selected for further analysis in the text.

For an experimental system at equilibrium, the free energy—Helmholtz, F, (if number of moles, volume, and temperature are kept constant) or Gibbs, G, (if number of moles, pressure and temperature are controlled)—is minimized. When a system contains multiple phases, the interface separates these phases from one another, given sufficiently low activation energies and sufficient time. The interface region, coined the interphase, contains all the inhomogeneity and nonuniformity between the bulk phases. The interface contributes to the free energy through the surface area term, in addition to having its own entropic and chemical potential terms. Using the surface excess approach for two phases,  $\alpha$  and  $\beta$ , an interface,  $\sigma$ , exists between them. The total free energy is the sum of each phase:

$$dF = dF^{\alpha} + dF^{\beta} + dF^{\sigma} \tag{5}$$

MD simulations capture the total energy differences as

$$E_{system} = E_{phase \,\alpha} + E_{phase \,\beta} + E_{interface} \tag{6}$$

Rearranging Eqn. 6, we obtain,

$$E_{interface} = E_{system} - E_{phase \alpha} - E_{phase \beta}$$
 (7)

In the MD simulations, entropy contributions are difficult to capture and typically small in vacuum.<sup>53</sup> Therefore, the energy differences obtained here are a good approximation for free energy differences. However, entropy differences can become significant upon phase changes such

as solvation.<sup>66</sup> Eqn. 7 was modified to find the approximate energy of lithium inclusion in the alumina network:

$$E_{Li\,inclusion} = E_{Li-Al-O\,system} - \left(E_{LCO\,surface} + E_{Al-O\,surface}\right) \tag{8}$$

where E<sub>Li-Al-O</sub> system is the total energy of the film-LCO system, E<sub>LCO</sub> surface is the total energy of the LCO slab, and E<sub>Al-O</sub> surface is the total energy of the amorphous Al-O film after deleting the Li atoms from the structure.

The result of Eqn. 8 for each simulation system is plotted as Figure 3a. We observe that it is favorable to incorporate lithium into the alumina lattice across all monolayer numbers. The average energy of lithium inclusion in the Al-O film is -109 mJ m<sup>-2</sup> Li atom<sup>-1</sup>  $\pm$  5 mJ m<sup>-2</sup> Li atom<sup>-1</sup> (excluding the one- and two-monolayer systems from the average). The energetic favorability for Li inclusion plateaus by three monolayers, which suggests that there is a critical thickness where the Al-O structure benefits the most from Li inclusion. We posit that one and two monolayer systems have higher (less favorable) Li incorporation energies because they are very thin films (< 1 nm) and, from a mechanical standpoint, have less strain to relieve than thicker films like the five-monolayer system. The 10-monolayer system is a thick film that has begun exhibiting a pure Al-O region; interestingly, it has a slightly higher average Li incorporation energy with large standard deviation. We conjecture that the lattice matching benefits of a Li-Al-O region begin to be outweighed by the disordered Al-O region. As a comparison, annealed wet chemical alumina films that exhibited an  $\alpha$ -LiAlO2 phase on LiCoO2 were 7 nm thick.<sup>24</sup>

Additionally, we verified that a 10-monolayer film with a partial Li distribution is the lowest energy structure. Figure 3b-3f provides a visual summary of the systems investigated. Elemental mass density profiles were averaged from the last 500 ps of all simulations and are also shown. From the Li-Al-O replicates, lithium extends through the film for about 2-2.5 nm from

the LCO surface. The average Li mass density profiles verify that the Al-O structure has minimal lithium distribution, and the homogenous Li-Al-O lattice has a uniform lithium distribution. Figure 3g plots the film energies of the last 500 ps of all 10-monolayer trajectories. Interestingly, the 10-monolayer structures at the extremes of Li distribution had the most unfavorable energies, while the Li-Al-O replicates—which captured partial lithium distributions through the film—had the most favorable energies. Li-Al-O replicate 1 possessed the lowest system energy and is further analyzed in this work.

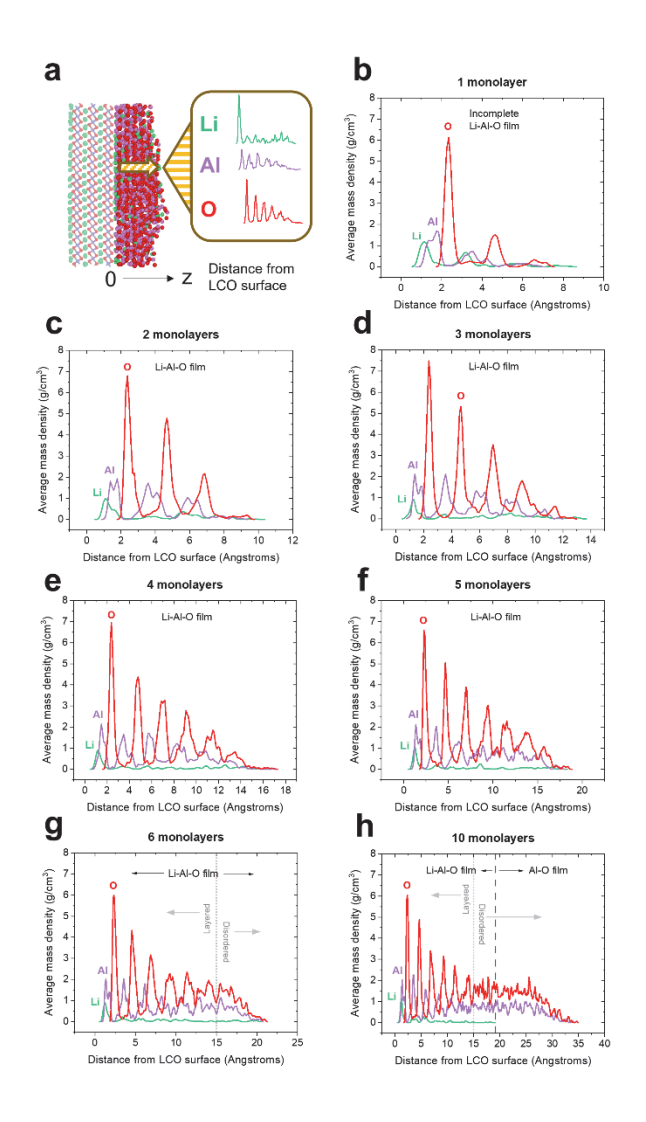


**Figure 4.** Elemental mass density profiles of the film calculated in the z-direction away from the LiCoO<sub>2</sub> surface. (a) Graphical representation of how the elemental mass densities were calculated through the Li-Al-O films. Lithium is in green, aluminum is in purple, and oxygen is in red. (b-h) The mass density profiles were averaged over the entire 1000-frame trajectories. The well-defined peaks of Al and O near the LCO surface indicate aluminum and oxygen layering. (g-h) This Al and O layering extends for about 1.5 nm before transitioning to a disordered structure. (h) The Li-Al-O region extends for about 2 nm from the LCO surface before transitioning to a lithium-free, Al-O region at the film surface.

We quantified the nanostructure of our simulated films by calculating the mass density profiles of the lithium, aluminum, and oxygen using the density profile tool for VMD.<sup>54</sup> Figure 4 summarizes the mass density profiles calculated in the z-direction away from the LiCoO<sub>2</sub> surface.

Interestingly, we observe layering of the aluminum and oxygen near the LiCoO<sub>2</sub> surface that extends for about five aluminum layers and six oxygen layers. This layered region extends for about 15 Angstroms (1.5 nm) before transitioning to a disordered structure. Moreover, in Figure 4h, we observe a transition from a Li-Al-O region to an Al-O region around 20 Angstroms. Table S3 provides the first peak integration for the Li, Al, and O mass density profiles. The first peak integration is directly proportional to the amount of that element present at the interface between the LiCoO<sub>2</sub> sheet and the amorphous film. The amount of interfacial lithium is relatively constant across the 2- to 6- and 10-monolayer systems and ranges between 36% - 46% of the total lithium present throughout the Li-Al-O film.

Hoskins et al. already experimentally provided evidence for the formation of a Li-Al-O region between the cathode active material and Al<sub>2</sub>O<sub>3</sub>. Our six-monolayer and 10-monolayer simulations contain a Li-Al-O region before transitioning to a disordered, mostly or completely lithium-free Al-O region. Our simulations support the hypothesis that the interface between the ALD Al<sub>2</sub>O<sub>3</sub> – LiMO<sub>2</sub> system is a reactive interface that forms a Li-Al-O compound. We can consider this Li-Al-O region a pseudomorphic layer<sup>64</sup> that approximately assumes the structure of the substrate rather than the pure, bulk alumina structure. From our MD simulations, we surmise the Li-Al-O interphase is about 2 nm thick before transitioning to an Al-O film. This simulated, outer, amorphous Al-O film has experimental corroboration: sufficiently thick (~3 nm) experimental Al<sub>2</sub>O<sub>3</sub> ALD films on Li<sub>1.2</sub>Ni<sub>0.13</sub>Mn<sub>0.54</sub>Co<sub>0.13</sub>O<sub>2</sub> do not have a Li-Al-O phase present at the surface, as determined by XPS.<sup>20</sup>

#### 3.2 Coordination environment

**Table 1.** Experimental and computed bond lengths for Al-O, O-O, and O-Li of lithium aluminates and amorphous Li-Al-O and Al-O systems.

	Bond length (Å)		
System	Al-O	O-O	O-Li
α-LiAlO <sub>2</sub> (Poeppelmeier et al., 1988) <sup>67</sup>	1.926	2.647, Al-O sheet 3.087, Li-O sheet	2.084
γ-LiAlO <sub>2</sub> (Marezio, 1965) <sup>68</sup>	1.761	2.856, tetrahedron about Al 3.191, tetrahedron about Li	2.00
This work, Li-Al-O region <sup>a</sup>	$1.78 \pm 0.11$	$2.80 \pm 0.20$	$1.79 \pm 0.14$
This work, Al-O region <sup>b</sup>	$1.75 \pm 0.11$	$2.75 \pm 0.25$	N/A
Amorphous Al <sub>2</sub> O <sub>3</sub> (Lamparter & Kniep, 1997) <sup>69</sup>	$1.8 \pm 0.21$	$2.8 \pm 0.58$	N/A
Amorphous Al <sub>2</sub> O <sub>3</sub> , MD simulation (Gutiérrez & Johansson, 2002) <sup>70</sup>	$1.76 \pm 0.1$	$2.75\pm0.2$	N/A

<sup>&</sup>lt;sup>a</sup>The bond lengths of the Li-Al-O region were averaged from the 2- to 6- and 10-monolayer systems.

The local order of the simulated films was further analyzed by computing the bond lengths and atom coordination numbers. This work's Al-O and O-O bond lengths in Table 1 match prior experiments and simulations of amorphous Al<sub>2</sub>O<sub>3</sub> quite well.<sup>68-70</sup> The bond lengths were calculated from averages of two regions: Li-Al-O (which included the two-, three-, four-, five-, and six-monolayer films and part of the 10-monolayer film) and Al-O, which was only found in part of the 10-monolayer simulation. The simulated one-monolayer system nor the film surface atoms of the other systems were included in the bond length analysis. The Al-O and O-O bond lengths (1.78 Å  $\pm$  0.11 Å and 2.80 Å  $\pm$  0.20 Å, respectively) of the Li-Al-O region are smaller than the bond lengths of crystalline  $\alpha$ -LiAlO<sub>2</sub>, which suggests that while the Li-Al-O region exhibits Al and O layering

<sup>&</sup>lt;sup>b</sup>The bond lengths of the Al-O region were from the 10-monlayer system.

in the z-direction (as shown in Figure 3), this region is not a proper  $\alpha$ -LiAlO<sub>2</sub> phase. Additionally, the Al-O and O-O bonds are similar in length to the Al-O bond length of  $\gamma$ -LiAlO<sub>2</sub> (and O-O bond if one only considers the AlO<sub>4</sub> tetrahedron). Moreover, the Al-O and O-Li bonds of this Li-Al-O region are also quite similar in length (1.78 Å  $\pm$  0.11 Å versus 1.79 Å  $\pm$  0.14 Å), which implies the Li-Al-O structure has Al and Li residing in similar sites around O.

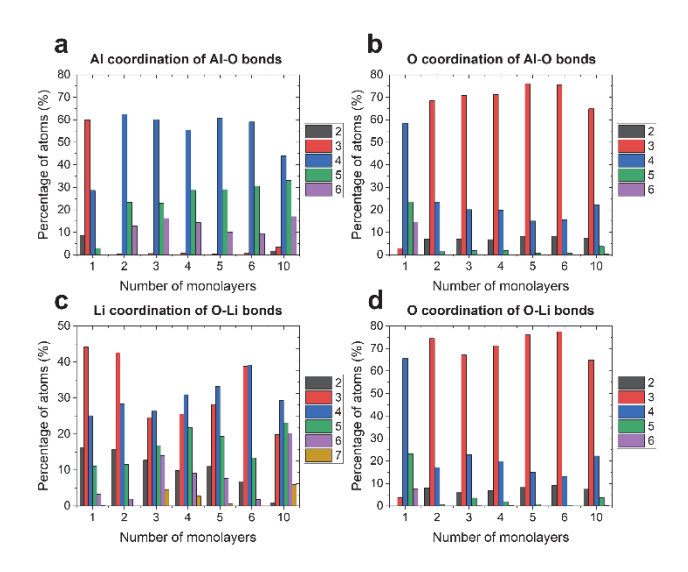


Figure 5. The percentage of elements with a certain coordination number for each simulated film. The percentage of Al and O coordination numbers across monolayers is relatively unchanged while there is spread in the percentage of lithium coordination numbers. These trends indicate that Li is quite mobile in the stable, amorphous Al-O structure. All atom percentages are averaged every 100 frames for the entire 1000 frame trajectories. The standard deviation is not shown but is ±1-5%, with Li having the largest standard deviations. Because the 1-monolayer system is not a fully formed film, its coordination environment differs from the other monolayer systems. (a) The distribution of Al coordination numbers for the Al-O bond. The most common coordination environment for Al is <sup>[4]</sup>Al, followed by <sup>[5]</sup>Al, and then <sup>[6]</sup>Al. (b) The O coordination numbers for the Al-O bond. The large spread in coordination number suggests that Li adopts many configurations in the Li-Al-O lattice. (d) The O coordination numbers for the O-Li bond are similar to the O coordination for the Al-O bond.

The averaged coordination numbers for each monolayer system are shown in Figure 5. In Figure 5a, b, and d, the one monolayer system is not a fully formed film and as a result, has undercoordinated Al (primarily <sup>[2]</sup>Al and <sup>[3]</sup>Al) and over-coordinated O (significant amounts of <sup>[4]</sup>O and considerable amounts of <sup>[5]</sup>O and <sup>[6]</sup>O). This result suggests incomplete or nucleating films need to be stabilized with other surface species while the film lattice is being established. Of the fully formed films, the amounts of Al and O coordination are stable; the general trend is <sup>[4]</sup>Al > <sup>[5]</sup>Al > <sup>[6]</sup>Al and predominantly <sup>[3]</sup>O. The oxygen coordination for both Al-O and O-Li bonds is extremely

similar, which further suggests that Al and Li occupy similar sites in relation to O. Li possesses the widest spread in coordination, as shown in Figure 5c. Lithium mainly exists as <sup>[3]</sup>Li and <sup>[4]</sup>Li, with standard deviations ranging between 3%-5% of Li atoms. The relatively unchanging Al and O coordination numbers across monolayers coupled with the wide spread of lithium coordination suggests that Li is quite mobile in the stable, amorphous Al-O structure.

**Table 2.** Coordination environments for crystalline alumina and lithium aluminates, as well as amorphous (A) alumina and Li-Al-O films.

System	Coordi	nation number (%	of atoms)
System	Al in Al-O	Li in O-Li	O in Al-O and O-Li
α-Al <sub>2</sub> O <sub>3</sub>	6 (100%)	N/A	4 (100%)
α-LiAlO <sub>2</sub>	6 (100%)	6 (100%)	6 (50% to Al, 50% to Li)
γ-LiAlO <sub>2</sub>	4 (100%)	4 (100%)	4 (50% to Al, 50% to Li)
This work, Li-Al-O region <sup>a</sup>	6 (13%) 5 (29%) 4 (56%) 3 (1%)	7 (2%) 6 (9%) 5 (18%) 4 (31%) 3 (30%) 2 (9%)	5 (2%) 4 (18%) 3 (72%) 2 (8%)
This work, Al-O region <sup>b</sup>	6 (3%) 5 (24%) 4 (62%) 3 (8%) 2 (3%)	N/A	4 (4%) 3 (75%) 2 (21%)
Amorphous (A) Al <sub>2</sub> O <sub>3</sub> on Si(100) at 200°C, plasma enhanced ALD (Lee et al., 2010) <sup>71</sup>	6 (5.1%) 5 (40.6%) 4 (54.3%)	N/A	Not reported
A-Al <sub>2</sub> O <sub>3</sub> Si <sub>3</sub> N <sub>4</sub> / Si(100) at 25°C, physical vapor deposition (Lee et al., 2010) <sup>71</sup>	6 (7.4%) 5 (36.2%) 4 (56.4%)	N/A	Not reported
A-Al <sub>2</sub> O <sub>3</sub> on Si(100) at 360°C, metal organic chemical vapor deposition (Sarou-Kanian et al., 2013) <sup>72</sup>	6 (26.2% ± 0.7%) 5 (40.9% ± 0.7%) 4 (32.9% ± 0.8%) avg. 4.93	N/A	Not reported

A-Al <sub>2</sub> O <sub>3</sub> on Si(100) at 720°C, metal organic chemical vapor deposition (Sarou-Kanian et al., 2013) <sup>72</sup>	6 (59.2% ± 0.5%) 5 (12.2% ± 0.6%) 4 (28.6% ± 0.6%) avg. 5.31	N/A	Not reported
A-Al <sub>2</sub> O <sub>3</sub> on NMC811 at 200°C, sol-gel coating (Riesgo-Gonzalez et al., 2022) <sup>17</sup>	6 (41%) 5 (21%) 4 (38%)	Not reported	Not reported
A-Al <sub>2</sub> O <sub>3</sub> on NMC811 at 600°C, sol-gel coating (Riesgo-Gonzalez et al., 2022) <sup>17</sup>	6 (24%) 5 (11%) 4 (65%)	Not reported	Not reported
A-Al <sub>2</sub> O <sub>3</sub> through anodic oxidation of Al foil, Reverse Monte Carlo simulation (Lamparter & Kniep, 1997) <sup>69</sup>	5 (22%) 4 (56%) 3 (20%)	N/A	Not reported
A-Al <sub>2</sub> O <sub>3</sub> , MD simulation (Gutiérrez & Johansson, 2002) <sup>70</sup>	6 (2%) 5 (22%) 4 (76%)	N/A	4 (2%) 3 (78%) 2 (20%)
A-Al <sub>2</sub> O <sub>3</sub> film, MD simulation (Adiga et al., 2006) <sup>73</sup>	6 (2%) 5 (20%) 4 (78%)	N/A	4 (2%) 3 (81%) 2 (17%)

<sup>&</sup>lt;sup>a</sup>The coordination numbers of the Li-Al-O region were averaged from the 2- to 6- and 10-monolayer systems.

Table 2 summarizes some reported Al, O, and Li coordination numbers from literature along with calculations from this work. In this work, the percentages of atoms exhibiting a particular coordination number were calculated for the Li-Al-O region by adding the number of atoms exhibiting a certain coordination number for each monolayer system and dividing by the total atoms of that type. Using the <sup>[4]</sup>Al coordination as an example, the averaged number <sup>[4]</sup>Al atoms (counted every 100 frames for 1000 frames) for the two- to six- and 10-monolayer systems were summed and divided by the total number of Al atoms (summed across two to six and 10

<sup>&</sup>lt;sup>b</sup>The coordination numbers of the Al-O region were from the 10-monlayer system.

monolayers). The Al-O region atom coordination percentages were calculated using the 10-monolayer system.

Crystal phases are included as references. For example,  $\alpha$ -LiAlO<sub>2</sub> contains only <sup>[6]</sup>Li while  $\gamma$ -LiAlO<sub>2</sub> contains only <sup>[4]</sup>Li. Additionally, <sup>[6]</sup>Al is the sole aluminum coordination environment of  $\alpha$ -Al<sub>2</sub>O<sub>3</sub> and  $\alpha$ -LiAlO<sub>2</sub> while  $\gamma$ -LiAlO<sub>2</sub> contains only <sup>[4]</sup>Al. As an aside,  $\gamma$ -Al<sub>2</sub>O<sub>3</sub> was not included because its structural characteristics have not been agreed upon by researchers, with groups proposing models ranging from cubic spinel-like to dehydrated non-spinel models. <sup>74</sup> The lack of consensus stems from the range of structural characteristics  $\gamma$ -Al<sub>2</sub>O<sub>3</sub> adopts depending on the starting synthesis material and the temperature of calcination. <sup>75, 76</sup> In fact,  $\gamma$ -Al<sub>2</sub>O<sub>3</sub> is the most disordered of the transition aluminas, <sup>76</sup> with some comparing its surface to amorphous Al<sub>2</sub>O<sub>3</sub>. <sup>70</sup> Additionally, pure crystalline alumina phases do not contain <sup>[5]</sup>Al, hence, <sup>[5]</sup>Al is solely attributed to the amorphous phase, <sup>17</sup> with Lee et al. going as far as to call the amount of <sup>[5]</sup>Al as the "degree of disorder in amorphous oxides."

Experimental diffraction data can be fit using atomistic models. Lamparter & Kniep fit a Reverse Monte Carlo (RMC) model to total pair correlation functions obtained by X-ray and neutron diffraction experiments on amorphous alumina films. Their RMC model determined their amorphous sample was primarily comprised of AlO<sub>4</sub> polyhedra, with minimal AlO<sub>6</sub>. Paranamana et al. fit RMC-molecular statics models to pair distribution functions obtained by electron diffraction data of ALD AlO<sub>x</sub> films.<sup>77</sup> They found the Al atoms had an average coordination number of 4.833 in the film bulk, which they attributed to a blend of tetrahedral and octahedral aluminum centers (AlO<sub>4</sub> and AlO<sub>6</sub>, respectively). We highlight the work of Lamparter & Kniep and Paranamana et al. to point out that even amorphous Al-O structures can have significant amounts of [4]Al.

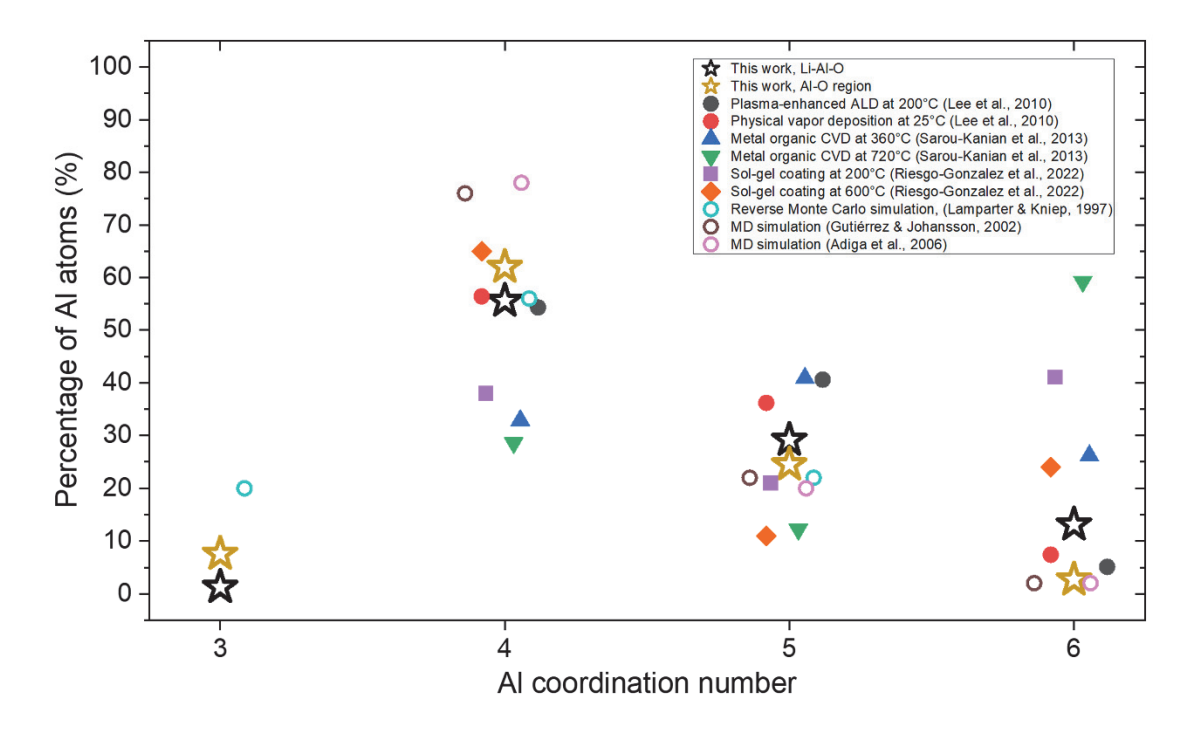


**Figure 6.** Experimentally measured and simulated aluminum coordination numbers in amorphous alumina films. Jitter in the x-direction was added to the scatter points to allow better readability. Although there is large variation within an Al coordination number, <sup>[4]</sup>Al is generally the prevailing coordination number. The amount of <sup>[6]</sup>Al depends on the film growth technique and temperature used while <sup>[5]</sup>Al is unique to amorphous alumina. <sup>[3]</sup>Al was only calculated in the simulated alumina films, most likely due the simulated surface Al being undercoordinated. The solid markers correspond to experimental measurements taken using solid-state <sup>27</sup>Al NMR spectroscopy while the empty markers correspond to simulated amorphous alumina films.

Figure 6 visualizes the experimentally measured aluminum coordination numbers along with some simulations listed in Table 2. The experimental processes to grow amorphous alumina films included physical vapor deposition (PVD), ALD, chemical vapor deposition (CVD), and solgel wet chemical coating. There is considerable spread within a coordination number (between ~30% - 60%); nevertheless, <sup>[4]</sup>Al is generally the most prevalent coordination environment. The amount of <sup>[6]</sup>Al depends on the process conditions and film deposition technique used. Simulated

amorphous Al<sub>2</sub>O<sub>3</sub> films expect the percentage of <sup>[6]</sup>Al to be low. <sup>[3]</sup>Al was not experimentally measured, but could be present at surfaces and interfaces, which differ from the bulk.<sup>73</sup>

The experimentally measured Al coordination environments should come with the caveat: they sample the bulk material or very thick films (hundreds or thousands of nanometers). However, our system investigates ultrathin alumina ALD films on layered transition metal oxides. Beneficial ALD films on these substrates are determined experimentally to be less than 2 nm thick;<sup>33</sup> our thickest simulated film is only ~3 nm thick. We expect these extremely thin films to be greatly influenced by their interfaces. This work follows the trend of predominant <sup>[4]</sup>Al established by the literature. The next question to consider is how the Al coordination changes through an ultrathin film.

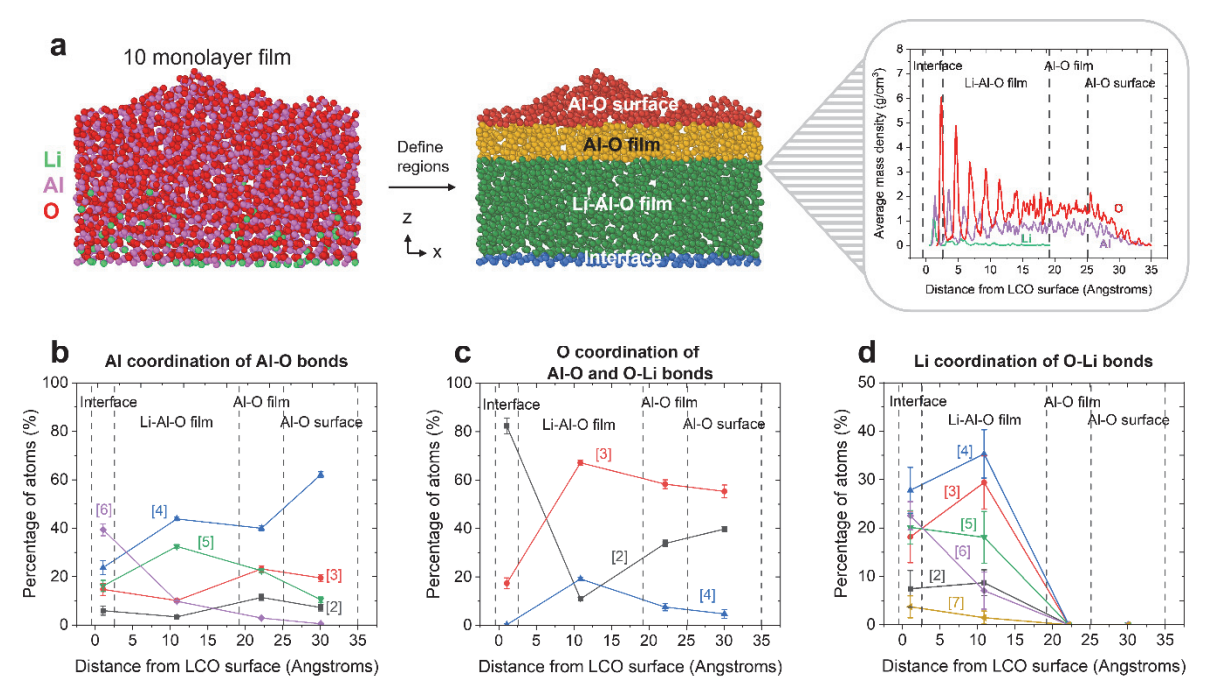


Figure 7. Coordination environment as a function of distance through the simulated 10-monolayer film. (a) The film was broken into four regions based on its mass density profile (the colors of the four regions were chosen to highlight the different regions and do not correspond to coordination numbers). The coordination numbers were calculated for each of the regions every 100 frames for 1000 frames and averaged. (b) Distribution of Al coordination numbers with O atoms for the Al-O bonds as a function of distance from the LCO surface. The highest percentage of [6]Al occurred in the interface region. Otherwise, [4]Al is the most common coordination environment, especially towards the outside of the film. (c) Distribution of O coordination numbers with the sum of Al and Li atoms for the Al-O and O-Li bonds as a function of distance from the LCO surface. Oxygen atoms in the film are undercoordinated at the interface, which we hypothesize is due to the presence of additional oxygen from the LiCoO<sub>2</sub> sheet. (d) Distribution of Li coordination numbers for the O-Li bonds as a function of distance from the surface. The large standard deviations indicate the Li coordination environment frequently changes. The Al-O film and Al-O surface regions do not contain any Li atoms.

Figure 7 represents the coordination environment as a function of distance through the film. The 10-monolayer system was investigated and broken into four subregions based on the mass density profile in Figure 4h and reprinted with region demarcations in Figure 7a. The 10-monolayer cutoffs used in Figure 5 were applied to each subregion. In the case of the 10-monolayer system, the cutoff for Al-O and O-Li bonds were the same at 2.45 Å. In Figure 7b, the majority of <sup>[6]</sup>Al occurs at the interface before decreasing to zero at the surface. The surface of the film is

mostly composed of <sup>[4]</sup>Al with a noticeable amount of <sup>[3]</sup>Al, which Adiga et al. also observed in their surface simulations.<sup>73</sup> Interestingly, in Figure 7c, oxygen is predominantly <sup>[2]</sup>O at the interface. We hypothesize the low coordination of film oxygen is due to the large oxygen presence from the LCO sheet, which was not included in any of this work's coordination analyses. The large standard deviations of Li In Figure 7d correlate to highly mobile Li atoms that switch coordination environments frequently. To note, the largest amount of <sup>[6]</sup>Li occurred at the interface subregion. The large percentage of <sup>[6]</sup>Al and <sup>[6]</sup>Li at the interface gives the film α-LiAlO<sub>2</sub> character and evidence for a heteroepitaxial Li-Al-O overlayer. LiCoO<sub>2</sub> possesses <sup>[6]</sup>Co and <sup>[6]</sup>Li bonding environments—and the proximity to the LCO sheet fosters this 6-fold coordination environment in the Li-Al-O film.

# 4. CONCLUSIONS

In summary, we have analyzed the nanostructure of amorphous Li-Al-O ALD-like films in contact with the (0001) LiCoO<sub>2</sub> surface using molecular dynamics simulations. We observe layering of Al and O atoms in the Li-Al-O region that extends for about 1.5 nm from the LCO surface before transitioning to a disordered Al-O structure. Lithium exists within the Al-O network for about 2 nm from the LCO surface. According to our simulations, the ALD film nanostructure differs from the  $\alpha$ -LiAlO<sub>2</sub> lattice matching arguments made for wet chemical alumina films: while the simulated ALD-like films possess layered Al-O sheets evocative of  $\alpha$ -LiAlO<sub>2</sub>, they contain very little <sup>[6]</sup>Al and have significant amounts of <sup>[4]</sup>Al. We note that <sup>[4]</sup>Al is associated with amorphous Al<sub>2</sub>O<sub>3</sub> and also  $\gamma$ -LiAlO<sub>2</sub>. The lack of <sup>[6]</sup>Al and prevalence of <sup>[4]</sup>Al suggests that the films are amorphous and function as pseudomorphic overlayers, where the Li-Al-O structure is inspired by the underlying layered LCO lattice but does not exactly replicate it. Furthermore, Li was found to be quite mobile through the Al-O network, with Li and Al occupying similar sites in

relation to oxygen. Because LiCoO<sub>2</sub> shares the same 3D space group  $(R\overline{3}m)$  as NMC, we expect the simulated results of the film nanostructure (that is, layering of Al and O atoms at the interface and the Li-Al-O region persisting for ~2 nm) to not change if NMC is used as the model surface. This computational study provides atomistic insight into the nanostructure of the alumina ALD film-LiMO<sub>2</sub> interface and supports the argument that Al<sub>2</sub>O<sub>3</sub> ALD films coat transition metal sites while allowing Li to intercalate through the film. Additionally, with the observation of the Li-Al-O film transitioning to a pure Al-O structure at sufficient thicknesses, this study provides rationale as to why low cycles of alumina ALD are most beneficial to the electrochemical performance of layered transition metal oxides for Li-ion battery applications.

# 5. ASSOCIATED CONTENT

# **Supporting Information**

Additional simulation details, experimental lattice vectors, integration of lithium mass density profiles, and cumulative and partial radial distribution functions for all simulated monolayer systems (PDF)

# 6. AUTHOR INFORMATION

# **Corresponding authors**

Alan W. Weimer – Department of Chemical and Biological Engineering, University of Colorado Boulder, Boulder, Colorado 80309, United States; Email: <a href="mailto:alan.weimer@colorado.edu">alan.weimer@colorado.edu</a>; Orcid ID: 0000-0002-2471-349X

Hendrik Heinz – Department of Chemical and Biological Engineering, University of Colorado Boulder, Boulder, Colorado 80309, United States; Email: <a href="mailto:hendrik.heinz@colorado.edu">hendrik.heinz@colorado.edu</a>; Orcid ID: 0000-0002-6776-7404

# **Authors**

Julie A. Nguyen – Department of Chemical and Biological Engineering, University of Colorado Boulder, Boulder, Colorado 80309, United States; Orcid ID: 0000-0002-6286-9428

Abigayle Becker – Department of Chemical and Biological Engineering, University of Colorado Boulder, Boulder, Colorado 80309, United States

Krishan Kanhaiya – Department of Chemical and Biological Engineering, University of Colorado Boulder, Boulder, Colorado 80309, United States; Orcid ID: 0000-0002-3622-2655

# **Conflicts of interest**

The authors declare the following competing financial interests: A.W. W. has a significant financial interest in Forge Nano.

# 7. ACKNOWLEDGEMENTS

This material is based upon work supported by the National Science Foundation Graduate Research Fellowship under Grant No. 2040434 and the National Science Foundation under Grant No. OAC 1931587. This work utilized the Summit supercomputer, which is supported by the National Science Foundation (awards ACI-1532235 and ACI-1532236), the University of Colorado Boulder, and Colorado State University. The Summit supercomputer is a joint effort of the University of Colorado Boulder and Colorado State University. Additionally, this work utilized the Alpine high performance computing resource at the University of Colorado Boulder. Alpine is

jointly funded by the University of Colorado Boulder, the University of Colorado Anschutz, Colorado State University, and the National Science Foundation (award 2201538). J. A. N. gratefully acknowledges Jordan Winetrout for tutelage in automating the simulation workflow, Dr. Tesia Janicki, Dr. Samuel Marks, Dr. Matthew Weimer, Dr. Jamie DuMont, Dr. Christopher Gump, and Dr. Markus Groner for insightful discussions, Dr. Kent Warren for mentorship and manuscript feedback, and Jasmine Gabor and Dr. Gregory Pach for manuscript feedback.

#### 8. REFERENCES

- (1) Manthiram, A. A Reflection on Lithium-Ion Battery Cathode Chemistry. *Nat. Commun.* **2020**, *11* (1). DOI: 10.1038/s41467-020-15355-0.
- (2) Edge, J. S.; O'Kane, S.; Prosser, R.; Kirkaldy, N. D.; Patel, A. N.; Hales, A.; Ghosh, A.; Ai, W. L.; Chen, J. Y.; Yang, J.; et al. Lithium Ion Battery Degradation: What You Need to Know. *Phys. Chem. Chem. Phys.* **2021**, *23* (14), 8200-8221. DOI: 10.1039/d1cp00359c.
- (3) Li, W. D.; Erickson, E. M.; Manthiram, A. High-Nickel Layered Oxide Cathodes for Lithium-Based Automotive Batteries. *Nat. Energy* **2020**, *5* (1), 26-34. DOI: 10.1038/s41560-019-0513-0.
- (4) Jung, S. K.; Gwon, H.; Hong, J.; Park, K. Y.; Seo, D. H.; Kim, H.; Hyun, J.; Yang, W.; Kang, K. Understanding the Degradation Mechanisms of LiNi<sub>0.5</sub>Co<sub>0.2</sub>Mn<sub>0.3</sub>O<sub>2</sub> Cathode Material in Lithium Ion Batteries. *Adv. Energy Mater.* **2014**, *4* (1). DOI: 10.1002/aenm.201300787.
- (5) Jung, R.; Metzger, M.; Maglia, F.; Stinner, C.; Gasteiger, H. A. Oxygen Release and Its Effect on the Cycling Stability of LiNi<sub>x</sub>Mn<sub>y</sub>Co<sub>z</sub>O<sub>2</sub> (NMC) Cathode Materials for Li-Ion Batteries. *J. Electrochem. Soc.* **2017**, *164* (7), A1361-A1377. DOI: 10.1149/2.0021707jes.
- (6) Lim, J. M.; Hwang, T.; Kim, D.; Park, M. S.; Cho, K.; Cho, M. Intrinsic Origins of Crack Generation in Ni-rich LiNi<sub>0.8</sub>Co<sub>0.1</sub>Mn<sub>0.1</sub>O<sub>2</sub> Layered Oxide Cathode Material. *Sci. Rep.* **2017**, 7. DOI: 10.1038/srep39669.
- (7) Liu, W.; Oh, P.; Liu, X.; Lee, M. J.; Cho, W.; Chae, S.; Kim, Y.; Cho, J. Nickel-Rich Layered Lithium Transition-Metal Oxide for High-Energy Lithium-Ion Batteries. *Angew. Chem. Int. Edit.* **2015**, *54* (15), 4440-4457. DOI: 10.1002/anie.201409262.
- (8) Zhao, S.; Wang, B. Y.; Zhang, Z. H.; Zhang, X.; He, S. M.; Yu, H. J. First-Principles Computational Insights into Lithium Battery Cathode Materials. *Electrochem. Energy Rev.* **2022**, *5* (1), 1-31. DOI: 10.1007/s41918-021-00115-5.
- (9) Myung, S. T.; Maglia, F.; Park, K. J.; Yoon, C. S.; Lamp, P.; Kim, S. J.; Sun, Y. K. Nickel-Rich Layered Cathode Materials for Automotive Lithium-Ion Batteries: Achievements and Perspectives. *ACS Energy Lett.* **2017**, *2* (1), 196-223. DOI: 10.1021/acsenergylett.6b00594.
- (10) Birkl, C. R.; Roberts, M. R.; McTurk, E.; Bruce, P. G.; Howey, D. A. Degradation Diagnostics for Lithium Ion Cells. *J. Power Sources* **2017**, *341*, 373-386. DOI: 10.1016/j.jpowsour.2016.12.011.
- (11) Xie, J.; Sendek, A. D.; Cubuk, E. D.; Zhang, X. K.; Lu, Z. Y.; Gong, Y. J.; Wu, T.; Shi, F. F.; Liu, W.; Reed, E. J.; et al. Atomic Layer Deposition of Stable LiAlF<sub>4</sub> Lithium Ion Conductive Interfacial Layer for Stable Cathode Cycling. *ACS Nano* **2017**, *11* (7), 7019-7027. DOI: 10.1021/acsnano.7b02561.
- (12) Jung, Y. S.; Cavanagh, A. S.; Dillon, A. C.; Groner, M. D.; George, S. M.; Lee, S. H. Enhanced Stability of LiCoO<sub>2</sub> Cathodes in Lithium-Ion Batteries Using Surface Modification by Atomic Layer Deposition. *J. Electrochem. Soc.* **2010**, *157* (1), A75-A81. DOI: 10.1149/1.3258274.
- (13) Yu, H.; He, X. Q.; Liang, X. H. AlF<sub>3</sub>-Al<sub>2</sub>O<sub>3</sub> ALD Thin-Film-Coated Li<sub>1.2</sub>Mn<sub>0.54</sub>Co<sub>0.13</sub>Ni<sub>0.13</sub>O<sub>2</sub> Particles for Lithium-Ion Batteries: Long-Term Protection. *ACS Appl. Mater. Inter.* **2022**, *14* (3), 3991-4003. DOI: 10.1021/acsami.1c20005.

- (14) Han, B. H.; Paulauskas, T.; Key, B.; Peebles, C.; Park, J. S.; Klie, R. F.; Vaughey, J. T.; Dogan, F. Understanding the Role of Temperature and Cathode Composition on Interface and Bulk: Optimizing Aluminum Oxide Coatings for Li-Ion Cathodes. *ACS Appl. Mater. Inter.* **2017**, *9* (17), 14769-14778. DOI: 10.1021/acsami.7b00595.
- (15) Wu, Y.; Manthiram, A. High Capacity, Surface-Modified Layered Li[Li<sub>(1-x)/3</sub>Mn<sub>(2-x)/3</sub>Ni<sub>x/3</sub>Co<sub>x/3</sub>]O<sub>2</sub> Cathodes with Low Irreversible Capacity Loss. *Electrochem. Solid-State Lett.* **2006**, *9* (5), A221-A224. DOI: 10.1149/1.2180528.
- (16) Han, B. H.; Key, B.; Lapidus, S. H.; Garcia, J. C.; Iddir, H.; Vaughey, J. T.; Dogan, F. From Coating to Dopant: How the Transition Metal Composition Affects Alumina Coatings on Ni-Rich Cathodes. *ACS Appl. Mater. Inter.* **2017**, *9* (47), 41291-41302. DOI: 10.1021/acsami.7b13597.
- (17) Riesgo-González, V.; Hall, D. S.; Marker, K.; Slaughter, J.; Wright, D. S.; Grey, C. P. Effect of Annealing on the Structure, Composition, and Electrochemistry of NMC811 Coated with Al<sub>2</sub>O<sub>3</sub> Using an Alkoxide Precursor. *Chem. Mater.* **2022**, *34* (21), 9722-9735. DOI: 10.1021/acs.chemmater.2c02580.
- (18) Neudeck, S.; Mazilkin, A.; Reitz, C.; Hartmann, P.; Janek, J.; Brezesinski, T. Effect of Low-Temperature Al2O3 ALD Coating on Ni-Rich Layered Oxide Composite Cathode on the Long-Term Cycling Performance of Lithium-Ion Batteries. *Sci. Rep.* **2019**, *9*. DOI: 10.1038/s41598-019-41767-0.
- (19) Wise, A. M.; Ban, C. M.; Weker, J. N.; Misra, S.; Cavanagh, A. S.; Wu, Z. C.; Li, Z.; Whittingham, M. S.; Xu, K.; George, S. M.; et al. Effect of Al<sub>2</sub>O<sub>3</sub> Coating on Stabilizing LiNi<sub>0.4</sub>Mn<sub>0.4</sub>Co<sub>0.2</sub>O<sub>2</sub> Cathodes. *Chem. Mater.* **2015**, *27* (17), 6146-6154. DOI: 10.1021/acs.chemmater.5b02952.
- (20) Zhang, X. F.; Belharouak, I.; Li, L.; Lei, Y.; Elam, J. W.; Nie, A. M.; Chen, X. Q.; Yassar, R. S.; Axelbaum, R. L. Structural and Electrochemical Study of Al<sub>2</sub>O<sub>3</sub> and TiO<sub>2</sub> Coated Li<sub>1.2</sub>Ni<sub>0.13</sub>Mn<sub>0.54</sub>Co<sub>0.13</sub>O<sub>2</sub> Cathode Material Using ALD. *Adv. Energy Mater.* **2013**, *3* (10), 1299-1307. DOI: 10.1002/aenm.201300269.
- (21) Mohanty, D.; Dahlberg, K.; King, D. M.; David, L. A.; Sefat, A. S.; Wood, D. L.; Daniel, C.; Dhar, S.; Mahajan, V.; Lee, M.; et al. Modification of Ni-Rich FCG NMC and NCA Cathodes by Atomic Layer Deposition: Preventing Surface Phase Transitions for High-Voltage Lithium-Ion Batteries. *Sci. Rep.* **2016**, *6*. DOI: 10.1038/srep26532.
- (22) Young, M. J.; Letourneau, S.; Warburton, R. E.; Dose, W. M.; Johnson, C.; Greeley, J.; Elam, J. W. High-Rate Spinel LiMn<sub>2</sub>O<sub>4</sub> (LMO) Following Carbonate Removal and Formation of Li-Rich Interface by ALD Treatment. *J. Phys. Chem. C* **2019**, *123* (39), 23783-23790. DOI: 10.1021/acs.jpcc.9b04418.
- (23) Han, B. H.; Key, B.; Lipton, A. S.; Vaughey, J. T.; Hughes, B.; Trevey, J.; Dogan, F. Influence of Coating Protocols on Alumina-Coated Cathode Material: Atomic Layer Deposition versus Wet-Chemical Coating. *J. Electrochem. Soc.* **2019**, *166* (15), A3679-A3684. DOI: 10.1149/2.0681915jes.
- (24) Zheng, J. H.; Wang, Y.; Qin, M. M.; Sun, L. D.; Peng, C.; Li, Y.; Feng, W. Epitaxial Growth of a Single Hexagonal Layered α-LiAlO<sub>2</sub> Coating on a High-Voltage LiCoO<sub>2</sub> Cathode Material for Enhanced Stability. *J. Mater. Chem. A* **2023**, *11* (19), 10297-10308. DOI: 10.1039/d3ta01136d.

- (25) Riley, L. A.; Van Ana, S.; Cavanagh, A. S.; Yan, Y. F.; George, S. M.; Liu, P.; Dillon, A. C.; Lee, S. H. Electrochemical Effects of ALD Surface Modification on Combustion Synthesized LiNi<sub>1/3</sub>Mn<sub>1/3</sub>Co<sub>1/3</sub>O<sub>2</sub> as a Layered-Cathode Material. *J. Power Sources* **2011**, *196* (6), 3317-3324. DOI: 10.1016/j.jpowsour.2010.11.124.
- (26) Tebbe, J. L.; Holder, A. M.; Musgrave, C. B. Mechanisms of LiCoO<sub>2</sub> Cathode Degradation by Reaction with HF and Protection by Thin Oxide Coatings. *ACS Appl. Mater. Inter.* **2015**, *7* (43), 24265-24278. DOI: 10.1021/acsami.5b07887.
- (27) Darapaneni, P.; Mane, A. U.; Turczynski, A.; Elam, J. W. Elucidating the Redox Behavior during Atomic Layer Deposition on Lithium-Ion Battery Cathode Materials. *Chem. Mater.* **2021**, *33* (20), 8079-8088. DOI: 10.1021/acs.chemmater.1c02632.
- (28) Yu, H.; Gao, Y.; Kirtley, J.; Borgmeyer, G.; He, X. Q.; Liang, X. H. Recovery of Degraded Ni-Rich NMC811 Particles for Lithium-Ion Batteries. *J. Electrochem. Soc.* **2022**, *169* (5). DOI: 10.1149/1945-7111/ac6c56.
- (29) Zhao, Z.; Huang, G. S.; Kong, Y.; Cui, J. Z.; Solovev, A. A.; Li, X. F.; Mei, Y. F. Atomic Layer Deposition for Electrochemical Energy: from Design to Industrialization. *Electrochem. Energy Rev.* **2022**, *5* (Suppl 1). DOI: 10.1007/s41918-022-00146-6.
- (30) Puurunen, R. L. Surface Chemistry of Atomic Layer Deposition: A Case Study for the Trimethylaluminum/Water Process. *J. Appl. Phys.* **2005**, *97* (12). DOI: 10.1063/1.1940727.
- (31) Weimer, A. W. Particle Atomic Layer Deposition. *J. Nanopart. Res.* **2019**, *21* (1). DOI: 10.1007/s11051-018-4442-9.
- (32) van Ommen, J. R.; Goulas, A. Atomic Layer Deposition on Particulate Materials. *Mater. Today Chem.* **2019**, *14*. DOI: 10.1016/j.mtchem.2019.08.002.
- (33) Hoskins, A. L.; McNeary, W. W.; Millican, S. L.; Gossett, T. A.; Lai, A.; Gao, Y.; Liang, X. H.; Musgrave, C. B.; Weimer, A. W. Nonuniform Growth of Sub-2 Nanometer Atomic Layer Deposited Alumina Films on Lithium Nickel Manganese Cobalt Oxide Cathode Battery Materials. *ACS Appl. Nano Mater.* **2019**, *2* (11), 6989-6997. DOI: 10.1021/acsanm.9b01490.
- (34) Liu, Y.; Hudak, N. S.; Huber, D. L.; Limmer, S. J.; Sullivan, J. P.; Huang, J. Y. In Situ Transmission Electron Microscopy Observation of Pulverization of Aluminum Nanowires and Evolution of the Thin Surface Al<sub>2</sub>O<sub>3</sub> Layers during Lithiation-Delithiation Cycles. *Nano Lett.* **2011**, *11* (10), 4188-4194. DOI: 10.1021/nl202088h.
- (35) Aaltonen, T.; Nilsen, O.; Magraso, A.; Fjellvag, H. Atomic Layer Deposition of Li<sub>2</sub>O-Al<sub>2</sub>O<sub>3</sub> Thin Films. *Chem. Mater.* **2011**, *23* (21), 4669-4675. DOI: 10.1021/cm200899k.
- (36) Comstock, D. J.; Elam, J. W. Mechanistic Study of Lithium Aluminum Oxide Atomic Layer Deposition. *J. Phys. Chem. C* **2013**, *117* (4), 1677-1683. DOI: 10.1021/jp308828p.
- (37) Jung, S. C.; Han, Y. K. How Do Li Atoms Pass through the Al<sub>2</sub>O<sub>3</sub> Coating Layer during Lithiation in Li-ion Batteries? *J. Phys. Chem. Lett.* **2013**, 4 (16), 2681-2685. DOI: 10.1021/jz401231e.
- (38) Heinz, H.; Lin, T. J.; Mishra, R. K.; Emami, F. S. Thermodynamically Consistent Force Fields for the Assembly of Inorganic, Organic, and Biological Nanostructures: The INTERFACE Force Field. *Langmuir* **2013**, *29* (6), 1754-1765. DOI: 10.1021/la3038846.

- (39) Kanhaiya, K. Development and Application of Reliable Models for the Simulation of Metals and Oxides at the Nanoscale. Dissertation, University of Colorado at Boulder, Ann Arbor, 2022.
- (40) Dhakane, A.; Varshney, V.; Liu, J.; Heinz, H.; Jain, A. Molecular Dynamics Simulations of Separator-Cathode Interfacial Thermal Transport in a Li-Ion Cell. *Surf. Interfaces* **2020**, *21*. DOI: 10.1016/j.surfin.2020.100674.
- (41) Kanhaiya, K.; Heinz, H. Adsorption and Diffusion of Oxygen on Pure and Partially Oxidized Metal Surfaces in Ultrahigh Resolution. *Nano Lett.* **2022**. DOI: 10.1021/acs.nanolett.2c00490.
- (42) Kanhaiya, K.; Nathanson, M.; In 'T Veld, P. J.; Zhu, C.; Nikiforov, I.; Tadmor, E. B.; Choi, Y. K.; Im, W.; Mishra, R. K.; Heinz, H. Accurate Force Fields for Atomistic Simulations of Oxides, Hydroxides, and Organic Hybrid Materials up to the Micrometer Scale. *J. Chem. Theory Comput.* **2023**. DOI: 10.1021/acs.jctc.3c00750.
- (43) Kramer, D.; Ceder, G. Tailoring the Morphology of LiCoO<sub>2</sub>: A First Principles Study. *Chem. Mater.* **2009**, *21* (16), 3799-3809. DOI: 10.1021/cm9008943.
- (44) Gutierrez, A.; Choudhury, D.; Sharifi-Asl, S.; Yonemoto, B. T.; Shahbazian-Yassar, R.; Mane, A. U.; Elam, J. W.; Croy, J. Multifunctional Films Deposited by Atomic Layer Deposition for Tailored Interfaces of Electrochemical Systems. *J. Electrochem. Soc.* **2020**, *167* (14). DOI: 10.1149/1945-7111/abc768.
- (45) Bates, J. B.; Dudney, N. J.; Neudecker, B. J.; Hart, F. X.; Jun, H. P.; Hackney, S. A. Preferred Orientation of Polycrystalline LiCoO<sub>2</sub> Films. *J. Electrochem. Soc.* **2000**, *147* (1), 59-70. DOI: 10.1149/1.1393157.
- (46) Thompson, A. P.; Aktulga, H. M.; Berger, R.; Bolintineanu, D. S.; Brown, W. M.; Crozier, P. S.; in 't Veld, P. J.; Kohlmeyer, A.; Moore, S. G.; Nguyen, T. D.; et al. LAMMPS a Flexible Simulation Tool for Particle-Based Materials Modeling at the Atomic, Meso, and Continuum scales. *Comput. Phys. Commun.* **2022**, *271*, 108171. DOI: 10.1016/j.cpc.2021.108171.
- (47) Elam, J. W.; Groner, M. D.; George, S. M. Viscous Flow Reactor with Quartz Crystal Microbalance for Thin Film Growth by Atomic Layer Deposition. *Rev. Sci. Instrum.* **2002**, *73* (8), 2981-2987. DOI: 10.1063/1.1490410.
- (48) Sønsteby, H. H.; Yanguas-Gil, A.; Elam, J. W. Consistency and Reproducibility in Atomic Layer Deposition. *J. Vac. Sci. Technol. A* **2020**, *38* (2). DOI: 10.1116/1.5140603.
- (49) Liu, R.; Elleuch, O.; Wan, Z.; Zuo, P.; Janicki, T. D.; Alfieri, A. D.; Babcock, S. E.; Savage, D. E.; Schmidt, J. R.; Evans, P. G.; et al. Phase Selection and Structure of Low-Defect-Density γ-Al<sub>2</sub>O<sub>3</sub> Created by Epitaxial Crystallization of Amorphous Al<sub>2</sub>O<sub>3</sub>. *ACS Appl. Mater. Inter.* **2020**, *12* (51), 57598-57608. DOI: 10.1021/acsami.0c17606.
- (50) Hu, Z.; Shi, J.; Heath Turner, C. Molecular Dynamics Simulation of the Al<sub>2</sub>O<sub>3</sub> Film Structure during Atomic Layer Deposition. *Mol. Simul.* **2009**, *35* (4), 270-279. DOI: 10.1080/08927020802468372.
- (51) Bussi, G.; Donadio, D.; Parrinello, M. Canonical Sampling through Velocity Rescaling. *J. Chem. Phys.* **2007**, *126* (1), 014101. DOI: 10.1063/1.2408420.
- (52) Fu, Y.-T.; Heinz, H. Cleavage Energy of Alkylammonium-Modified Montmorillonite and Relation to Exfoliation in Nanocomposites: Influence of Cation Density, Head Group Structure, and Chain Length. *Chem. Mater.* **2010**, *22* (4), 1595-1605. DOI: 10.1021/cm902784r.

- (53) Mishra, R. K.; Flatt, R. J.; Heinz, H. Force Field for Tricalcium Silicate and Insight into Nanoscale Properties: Cleavage, Initial Hydration, and Adsorption of Organic Molecules. *J. Phys. Chem. C* **2013**, *117* (20), 10417-10432. DOI: 10.1021/jp312815g.
- (54) Giorgino, T. Computing 1-D Atomic Densities in Macromolecular Simulations: The Density Profile Tool for VMD. *Comput. Phys. Commun.* **2014**, *185* (1), 317-322. DOI: 10.1016/j.cpc.2013.08.022.
- (55) Stukowski, A. Visualization and Analysis of Atomistic Simulation Data with OVITO—The Open Visualization Tool. *Modelling Simul. Mater. Sci. Eng.* **2010**, *18* (1), 015012. DOI: 10.1088/0965-0393/18/1/015012.
- (56) Liu, J.; Zeng, J.; Zhu, C.; Miao, J. W.; Huang, Y.; Heinz, H. Interpretable Molecular Models for Molybdenum Disulfide and Insight into Selective Peptide Recognition. *Chem. Sci.* **2020**, *11* (33), 8708-8722. DOI: 10.1039/d0sc01443e.
- (57) Guerra-Nuñez, C.; Dobeli, M.; Michler, J.; Utke, I. Reaction and Growth Mechanisms in Al<sub>2</sub>O<sub>3</sub> Deposited via Atomic Layer Deposition: Elucidating the Hydrogen Source. *Chem. Mater.* **2017**, *29* (20), 8690-8703. DOI: 10.1021/acs.chemmater.7b02759.
- (58) Cho, D. H.; Jo, C. H.; Cho, W.; Kim, Y. J.; Yashiro, H.; Sun, Y. K.; Myung, S. T. Effect of Residual Lithium Compounds on Layer Ni-Rich Li[Ni<sub>0.7</sub>Mn<sub>0.3</sub>]O<sub>2</sub>. *J. Electrochem. Soc.* **2014**, *161* (6), A920-A926. DOI: 10.1149/2.042406jes.
- (59) Jung, R.; Morasch, R.; Karayaylali, P.; Phillips, K.; Maglia, F.; Stinner, C.; Shao-Horn, Y.; Gasteiger, H. A. Effect of Ambient Storage on the Degradation of Ni-Rich Positive Electrode Materials (NMC811) for Li-Ion Batteries. *J. Electrochem. Soc.* **2018**, *165* (2), A132-A141. DOI: 10.1149/2.0401802jes.
- (60) Groner, M. D.; Fabreguette, F. H.; Elam, J. W.; George, S. M. Low-Temperature Al<sub>2</sub>O<sub>3</sub> Atomic Layer Deposition. *Chem. Mater.* **2004**, *16* (4), 639-645. DOI: 10.1021/cm0304546.
- (61) George, S. M. Atomic Layer Deposition: An Overview. *Chem. Rev.* **2010**, *110* (1), 111-131. DOI: 10.1021/cr900056b.
- (62) Dingemans, G.; van de Sanden, M. C. M.; Kessels, W. M. M. Influence of the Deposition Temperature on the c-Si Surface Passivation by Al<sub>2</sub>O<sub>3</sub> Films Synthesized by ALD and PECVD. *Electrochem. Solid-State Lett.* **2010**, *13* (3), H76-H79. DOI: 10.1149/1.3276040.
- (63) Jin, Y.; Yu, H.; Liang, X. H. Understanding the Roles of Atomic Layer Deposition in Improving the Electrochemical Performance of Lithium-Ion Batteries. *Appl. Phys. Rev.* **2021**, 8 (3). DOI: 10.1063/5.0048337.
- (64) Kolasinski, K. W. Surface Science: Foundations of Catalysis and Nanoscience; John Wiley & Sons, Ltd., 2012.
- (65) Barnes, G. T.; Gentle, I. R. Interfacial Science: An Introduction; Oxford University Press, 2005.
- (66) Garley, A.; Hoff, S. E.; Saikia, N.; Jamadagni, S.; Baig, A.; Heinz, H. Adsorption and Substitution of Metal Ions on Hydroxyapatite as a Function of Crystal Facet and Electrolyte pH. *J. Phys. Chem. C* **2019**, *123* (27), 16982-16993. DOI: 10.1021/acs.jpcc.9b02808.

- (67) Poeppelmeier, K. R.; Chiang, C. K.; Kipp, D. O. Synthesis of High-Surface-Area α-LiAlO<sub>2</sub>. *Inorg. Chem.* **1988**, *27* (25), 4523-4524. DOI: 10.1021/ic00298a002.
- (68) Marezio, M. Crystal Structure and Anomalous Dispersion of  $\gamma$ -LiAlO<sub>2</sub>. *Acta Crystallogr.* **1965**, *19*, 396-&. DOI: 10.1107/S0365110x65003511.
- (69) Lamparter, P.; Kniep, R. Structure of Amorphous Al<sub>2</sub>O<sub>3</sub>. *Physica B* **1997**, *234*, 405-406. DOI: 10.1016/S0921-4526(96)01044-7.
- (70) Gutierrez, G.; Johansson, B. Molecular Dynamics Study of Structural Properties of Amorphous Al<sub>2</sub>O<sub>3</sub>. *Phys. Rev. B* **2002**, *65* (10). DOI: 10.1103/PhysRevB.65.104202.
- (71) Lee, S. K.; Park, S. Y.; Yi, Y. S.; Moon, J. Structure and Disorder in Amorphous Alumina Thin Films: Insights from High-Resolution Solid-State NMR. *J. Phys. Chem. C* **2010**, *114* (32), 13890-13894. DOI: 10.1021/jp105306r.
- (72) Sarou-Kanian, V.; Gleizes, A. N.; Florian, P.; Samelor, D.; Massiot, D.; Vahlas, C. Temperature-Dependent 4-, 5- and 6-Fold Coordination of Aluminum in MOCVD-Grown Amorphous Alumina Films: A Very High Field <sup>27</sup>Al-NMR study. *J. Phys. Chem. C* **2013**, *117* (42), 21965-21971. DOI: 10.1021/jp4077504.
- (73) Adiga, S. P.; Zapol, P.; Curtiss, L. A. Atomistic Simulations of Amorphous Alumina Surfaces. *Phys Rev B* **2006**, *74* (6). DOI: 10.1103/PhysRevB.74.064204.
- (74) Ayoola, H. O.; House, S. D.; Bonifacio, C. S.; Kisslinger, K.; Saidi, W. A.; Yang, J. C. Evaluating the Accuracy of Common  $\gamma$ -Al<sub>2</sub>O<sub>3</sub> Structure Models by Selected Area Electron Diffraction from High-Quality Crystalline  $\gamma$ -Al<sub>2</sub>O<sub>3</sub>. *Acta Mater.* **2020**, *182*, 257-266. DOI: 10.1016/j.actamat.2019.10.027.
- (75) Zhou, R. S.; Snyder, R. L. Structures and Transformation Mechanisms of the  $\eta$ ,  $\gamma$  and  $\theta$  Transition Aluminas. *Acta Crystallogr. B* **1991**, 47 (5), 617-630. DOI: 10.1107/s0108768191002719.
- (76) Stuart, N. M.; Sohlberg, K. The Microstructure of γ-Alumina. *Energies* **2021**, *14* (20), 6472. DOI: 10.3390/en14206472.
- (77) Paranamana, N. C.; Gettler, R.; Koenig, H.; Montgomery-Smith, S.; He, X. Q.; Young, M. J. Measuring Local Atomic Structure Variations through the Depth of Ultrathin (< 20 nm) ALD Aluminum Oxide: Implications for Lithium-Ion Batteries. *ACS Appl. Nano Mater.* **2022**, *5* (9), 12582-12591. DOI: 10.1021/acsanm.2c02312.

# FOR TABLE OF CONTENTS ONLY

